CERN/LHCC 2000-016
CMS TDR 5 Addendum 1
21 February 2000

Addendum to the CMS Tracker TDR by the CMS Collaboration

Contents

1 Introduction **1**

1.1 Overview of the all-silicon layout 1

1.2 The motivation for changing the baseline design 6

2 Sensors **9**

2.1 Sensor specifications 9

2.2 Comparisons between 6” and 4” prototypes 11

2.3 High voltage stability 11

2.4 Strip capacitances 12

2.5 Depletion voltage and charge collection efficiency 19

3 Module read-out and expected Signal to Noise Performance **21**

4 Modules **25**

4.1 Basic module layout 25

4.2 Modules assembly 26

4.3 Automated procedures and preliminary results 26

4.4 Burn-in test and repair 31

5 Mechanics, services and installation **33**

5.1 Support structure 33

5.2 Cooling and services 40

5.3 Detector assembly, installation and maintenance scenario 41

6 Performance **43**

6.1 Introduction . . . 43

6.2 Software . . . 43

6.3 Detector Layout . . . 43

6.4 Tracker Material Budget . . . 44

6.5 Single hit characteristics . . . 50

6.5.1 Hits in silicon micro-strip sensors . . . 50

6.5.2 Hits in MSGCs . . . 50

6.6 Occupancy . . . 54

6.7 Single Track Performance . . . 58

6.7.1 Track measurement precision . . . 58

6.7.2 Reconstruction efficiency . . . 61

6.8 Track Finding Efficiency in Jets . . . 65

6.9 Reconstruction of $B \to J/\psi K_S^0$ . . . 66

6.10 Reconstruction of converted photons . . . 67

6.11 Summary . . . 67

7 Organization of the Construction **71**

7.1 Cost estimate for the All-Silicon Tracker . . . 73

A Radiation environment and detector considerations **77**

1 Introduction

The detection and study of the diverse signatures for new physics at the LHC will rely on the clean identification and precise measurement of leptons, photons and jets. Robust tracking and detailed vertex reconstruction within a strong magnetic field are essential tools to reach these objectives. To meet these requirements, CMS proposed to build an inner silicon tracker, surrounded by an outer MSGC tracker, and with a pixel vertex detector close to the beam pipe.

At the time of the approval of the CMS Tracker TDR [1], in the spring of 1998, the robustness of the MSGC's in the aggressive LHC environment had yet to be established beyond doubt. Approval for construction was therefore made contingent on a large scale test, involving the exposure of dozens of chambers to an LHC-like beam, for a period of several weeks: the so-called "PSI Milestone". At the same time, the evolution of silicon strip sensors from a custom technology towards an industrialized one was being actively pursued. In the spring of 1999 the decision was taken to compare the baseline design with an all silicon back-up solution. The CMS steering committee meeting of 31 May 1999, however, recommended to investigate an all-silicon solution on equal footing. In December of 1999, the decision was taken to abandon the previous baseline design for the CMS Tracker, in favor of a tracking system based entirely on silicon detectors.

1.1 Overview of the all-silicon layout

The proposed all silicon tracker has approximately the same total number of readout channels, but somewhat less instrumented surface than the previous baseline layout: there are 10 rather than 11 barrel layers and 9 rather than 11 disks in each outer end-cap. Furthermore, the 5 stereo layers are now concentrated below a radius of 90 cm, whereas the previous baseline provided one additional stereo layer at a radius of 120 cm. Fig. 1 and Fig. 2 show two alternative layouts of the all-silicon tracker.

This reduction in surface was driven by budgetary constraints: as a result, the all silicon tracker is to very good approximation cost neutral with respect to the previous baseline layout. Simulations verify the expectation that, essentially due to the faster time response and better charge localization of silicon compared to the MSGC's, the tracking performance remains practically unchanged.

The all-silicon CMS tracker relies crucially on a few key elements. These are summarized below, and discussed in the following Sections.

The first key element is manufacturing sensors using 6" instead of 4" industrial production lines, of at least equal quality and high volume capacity. This will result in significant cost savings for the sensors and will also allow the use of large area modules in the outer part of the tracker. These

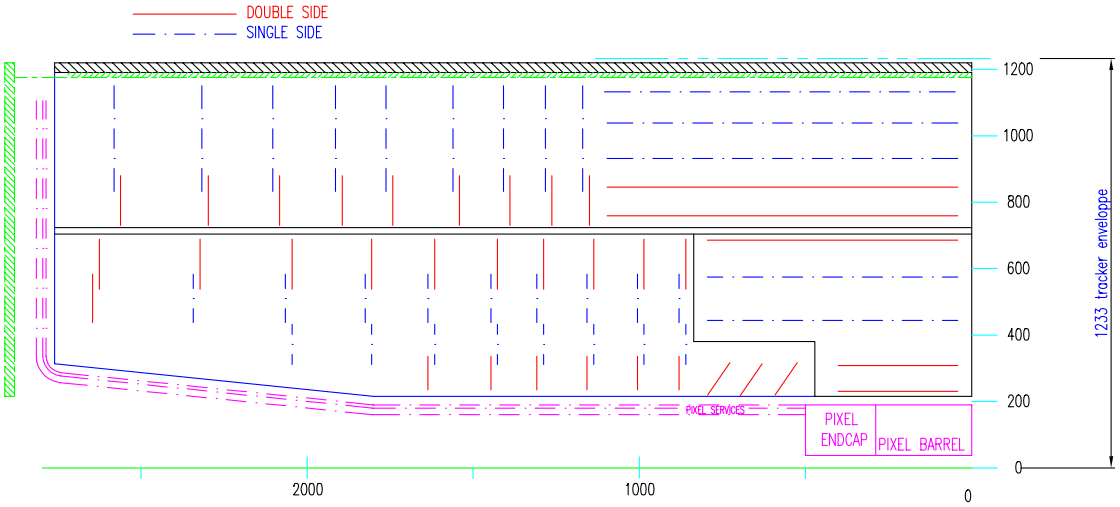

Figure 1: Longitudinal view of one quarter of a version of the all-silicon tracker which maintains the central support tube. Full lines = double-sided detectors, dashed-dotted lines = single-sided detectors.

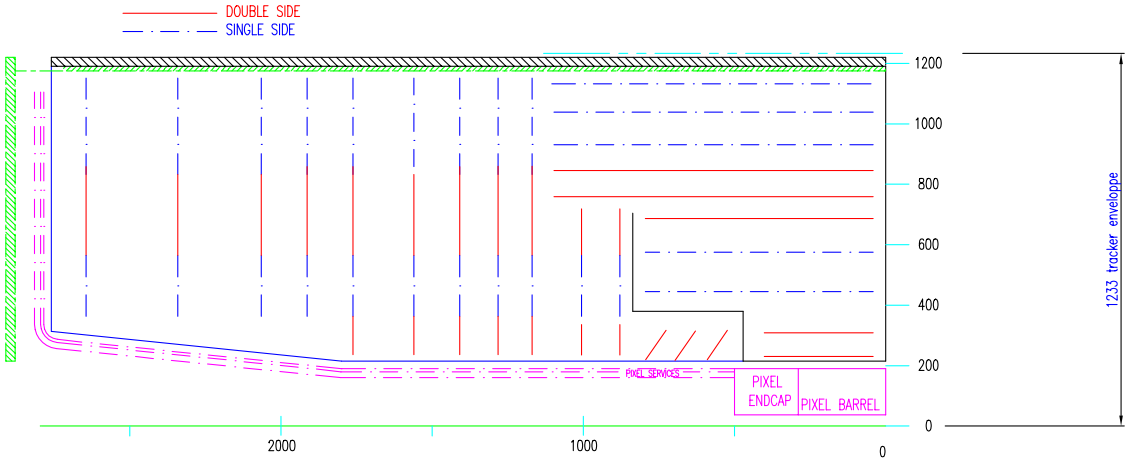

Figure 2: Longitudinal view of one quarter of a version of the all-silicon tracker without a central support tube. Full lines = double-sided detectors, dashed-dotted lines = single-sided detectors.

larger silicon modules are of comparable dimensions as the MSGC ones. Therefore, in the outer region there will be a similar number of both modules and read-out channels as initially foreseen.

Second is the substantial progress of a pilot project aimed at the automation of the previously difficult and time consuming steps of module assembly, as well as the possibility of exploiting the recent generation of high throughput wire bonding machines.

The third element is the successful implementation of the front-end read-out chip in deep sub-micron technology (APV25). This results both in a large cost saving and an improved S/N performance.

Finally, we rely on making extensive use of the studies performed so far on mechanical, thermal, electronic and other system aspects for both the inner silicon and the outer MSGC trackers, in order to provide well advanced starting points for the design of the all-silicon tracker. To that end, the performance of the all-silicon tracker has been evaluated with a layout which contains minimal changes with respect to the previous baseline design. Both the pixel and inner silicon tracker are left unchanged. The overall structure of the tracker, with a central support tube separating the inner and outer trackers is maintained (see Fig. 1). This is a conservative scenario.

The central support tube was a result of the requirement of providing well separated thermal volumes for the silicon and MSGC trackers: the first must operate at - 10^o, the second at approximately room temperature. In the all-silicon tracker, this constraint no longer exists. A study is underway to verify whether a different arrangement, with an external support tube and hermetic end-cap disks, may be a preferable arrangement to the present one. Such an arrangement would avoid the unfavorable radial gap in the end-cap disks, through which all cables and services for the inner tracker must otherwise be routed. Such a layout is sketched in Fig. 2. The implications of this on the modularity, installation and maintenance scenarios, as well as the additional engineering effort required are currently being evaluated.

For the outer tracker, modules will have dimensions of approximately 11×16 cm^2. They will be equipped with 6 and 4 APV25 chips (128 channels/chip) for the primary and stereo views respectively. For a module width of 11 cm this results in a read-out strip pitch of about 140 μm and 210 μm for the two views, yielding a point resolution of better than 40 μm and 60 μm for high p_T tracks. These resolutions compare well with those from the MSGCs, viz. 40 μm and 80 μm. The increased strip-length, 16 cm compared to 12 cm in the inner part of the tracker, is expected to increase the noise by 15 %. This will be compensated through the use of $\geq 400\mu$m thick sensors instead of the usual 300 μm thick ones, which will yield an increase of ≥ 30 % in the charge collection (see section 2.5).

The momentum resolution is, therefore, expected to be similar to that of the TDR layout, as can be seen in section 6. We do not expect any significant change in the impact parameter and b-

tagging performance as these are dominated by the characteristics of the pixel detector and the innermost silicon layers whose layout is not modified. Lastly, we expect that the material budget of the proposed system will be equal or lower with respect to the baseline proposal.

The outer barrel detector will have a length of about 2.25 m. Five detecting layers instrument the radial region between 0.75 and 1.15 m. Only layers 1 and 2 have back-to-back modules. Some overlap in z and r-phi among adjacent modules is foreseen. A total number of 2660 single-sided and 1372 back-to-back modules (for an equivalent number of 5404 single-sided modules) are needed to equip the outer barrel detector. The total area of silicon is 97.3 m^2 for a corresponding number of channels of 3.4 millions. Table 1 describes the main parameters of the outer barrel detector.

layer #	radius [mm]	pitch [μ m]	type	# of modules
1	750	140/210	back-to-back	644
2	850	140/210	back-to-back	728
3	950	140	single-sided	812
4	1050	140	single-sided	896
5	1150	140	single-sided	952

Table 1: Main parameters of the outer barrel detector.

Each outer end-cap disk is made-out of three rings of trapezoidal modules covering the radial region between 0.72 and 1.17 m (see Fig 3).

The first ring is made out of back-to-back modules. Nine disks are used for each side of the end-cap detector positioned at distances such that tracks crossing the outer tracker are measured at least five times for the entire eta coverage (see Figs. 1 and 2).

The total number of modules in the outer end-cap detector is 2124 single-sided and 828 back-to-back modules which translates into 3780 single-sided equivalent modules for a total number of 2.15 million channels and 67 m^2 of silicon. Table 2 summarizes the main parameters of the end-cap outer detector.

ring #	pitch [μ m]	type	# of modules
1	140/210	back-to-back	46
2	140	single-sided	54
3	140	single-sided	64

Table 2: Main parameters of one disk of the outer end-cap detector.

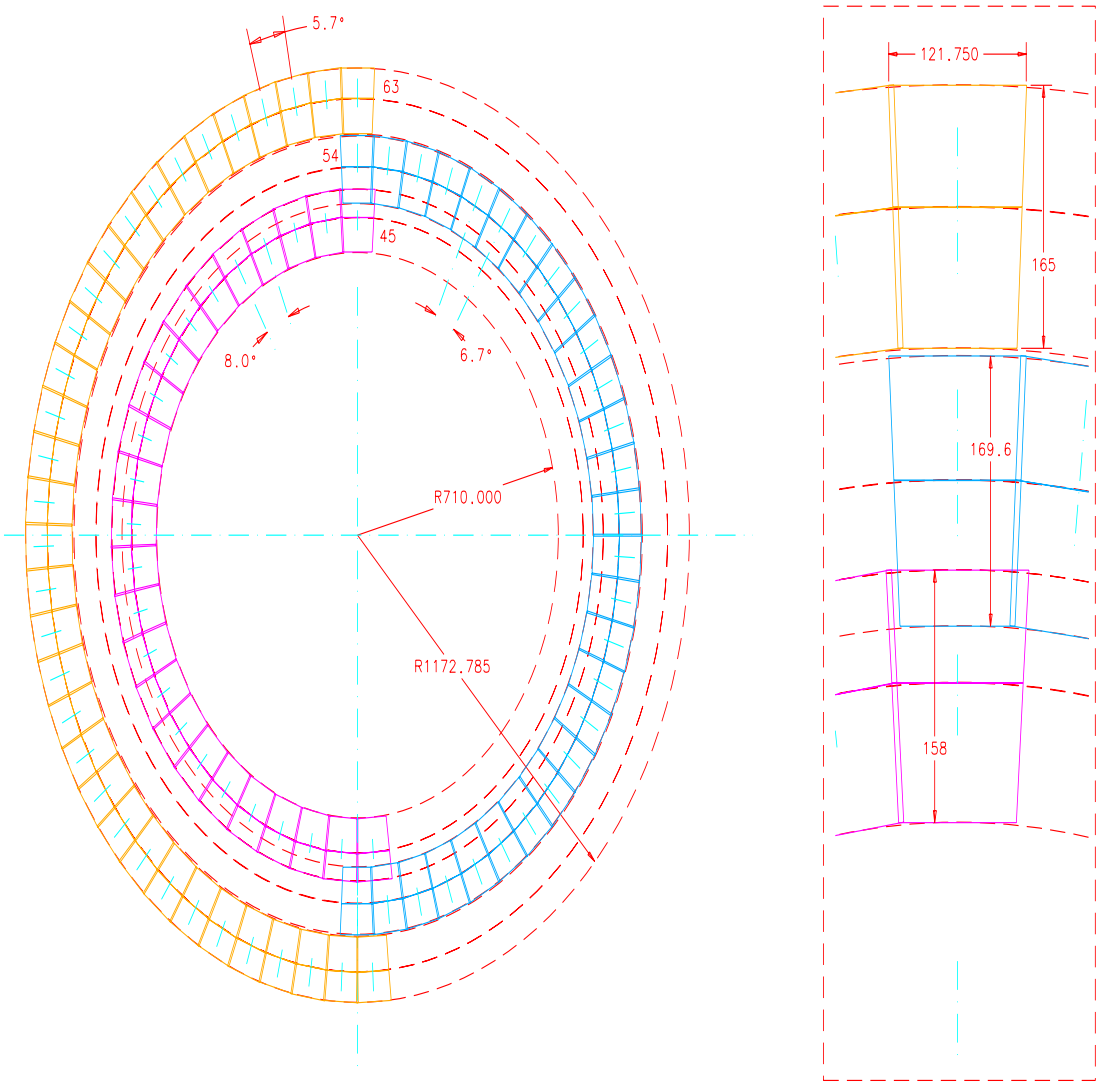

Figure 3: Layout of an end-cap disk. Dimensions on the right hand side are for the silicon sensors.

1.2 The motivation for changing the baseline design

During the spring of 1999, the decision was taken to study an all-silicon Tracker, as a back-up solution in case the results of the PSI milestone for the MSGC's turned out to be not fully satisfactory.

Based on the main new developments to be taken into consideration (the APV25 read-out chip, availability of 6" industrial lines for sensor production, and automation of module assembly), it became apparent that an all-silicon tracker of comparable performance to the baseline design might be shown to be within reach by the end of the year. As a result, in May 1999 it was decided to compare the two alternative options on an equal footing, during the internal review at the end of December.

In the fall of 1999, the large scale PSI Milestone test ($\sim$ 40 k strips exposed for 5 weeks) resulted in an unambiguous demonstration of the viability of the CMS MSGC's for tracking at the LHC. The barrel MSGC's (32 detectors), using the "advanced passivation" technique to protect all cathode edges, performed particularly well, giving clear evidence that these devices, produced in industry in a rather large quantity, can be safely operated at the LHC for more than 10 years. For the forward part of the CMS tracker a different construction, using unpassivated MSGC substrates (34 in the beam) and a GEM foil to provide a first stage of gain, was also shown to fulfill the milestone requirements. To work with a unified concept, the Forward MSGC community proposed to adopt the barrel design also for the forward part of the MSGC Tracker.

At the same time, the outstanding questions concerning the feasibility of an all silicon alternative were also answered positively. In particular, the expected performance of the APV25 (silicon version), the excellent quality of sensors manufactured on high volume industrial 6" production lines, as well as the possibility of streamlining module assembly through automation, were verified.

As a result, a review of the project at the end of December concluded that both the baseline and the all silicon options appeared to be technically feasible. The review, however, also highlighted the overall delay the project had incurred so far, for the construction of both the silicon and MSGC trackers, and raised significant concern about the ability of the collaboration to recover the lost time. This was the driving consideration behind the proposed change in design.

For both the silicon and MSGC projects, a program of work on aspects beyond the single module had been pursued over the past years, punctuated by a series of milestones. However, it is in these system aspects that the major remaining challenges of the project are to be found.

Moving from two "parallel" technologies to a single one was a unique opportunity to concentrate all available effort onto a reduced set of problems. This had to be weighted against both the obvious reluctance to abandon the MSGC technology at a time when its viability had been so successfully

established, and the inevitable time lost in reorganizing the community at this late stage of the project.

The decision was certainly a very difficult one, and strong arguments were given on both sides of the debate. Indeed, it was the opinion of the reviewers, and that of a large part of the tracker community itself, that abandoning the baseline design might cause too significant a disruption within the community for the project to benefit from the proposed change. As a result, a consensus could not be reached. The proposal by the Tracker Steering Committee to adopt the all silicon solution was eventually put to a vote, and endorsed by a minimal majority of the Tracker Institution Board.

The proposed new baseline has since been definitively endorsed by the CMS Collaboration, through a series of special meetings of its Steering Committee, Management Board and Collaboration Board.

The two months since this decision was taken have been very constructive. All groups in the CMS Tracker Collaboration are engaged in discussions aimed at redefining an appropriate share of responsibilities, and a revised project management structure matching it.

2 Sensors

2.1 Sensor specifications

Over the last few years considerable progress has been made in the understanding of the operation of silicon detectors in the harsh environment of the LHC. Among other results; (a) the interstrip capacitance remains unchanged after irradiation for $\langle 100 \rangle$ crystal lattice orientation, (b) the fluence at which type inversion takes place, and the required operational voltage after type-inversion, can be tuned by selecting the appropriate resisistivity, (c) the breakdown voltage can be considerably increased by use of appropriate readout strip and guard ring geometries.

The technology and specifications of the sensors for the outer part of the tracker are based on those already established for the inner part. Briefly, the sensors for the outer part are p-on-n devices with the following characteristics:

- The use of a substrate with $\langle 100 \rangle$ crystal lattice orientation;
- AC coupling of the metal read-out line to the implant strip;
- The use of polysilicon resistors to bias the strips;
- A ratio of strip width to pitch of $w/p = 0.25$;
- The use of metal overhang to enhance the breakdown performance;
- Standard edge treatment and an additional option of a multiguard structure, to be determined by the producer.

A number of parameters are adjusted to match the different requirements and operating conditions for the outer tracker. The modules for the outer barrel tracker consist of two identical rectangular daisy chained sensors, each 110 mm wide and 82.5 mm long. In the end-cap, the three rings are composed of modules made out of two trapezoidal daisy chained sensors with dimensions similar to those of the barrel. All designs are fully compatible with the design rules of several companies running 6" high volume processing lines. We envisage a minimum sensor thickness of 400 μm to increase the charge released by ionizing particles. With an initial resistivity of 3 kΩcm the depletion voltage before irradiation will be $\sim$ 190 V for a 400 μm thick detector. Under very conservative assumptions we predict a depletion voltage after 10 years of running to be below 150 V. Accounting for a factor 1.5 in overdepletion, to achieve the best possible signal-to-noise ratio, leads to an operating voltage of always less than 300 V. The requirement of an initial breakdown performance larger than 400 V still maintains a significant safety factor. Such a requirement is definitely looser with respect to the specifications required for the sensors in the inner part (breakdown voltage

Type	Crystal orientation	Resistivity (kΩ cm)	Thickness (μm)	Delivered prototypes
Multi-geometry	$\langle 111 \rangle$	$4 \div 8$	320	4
			375	2
			410	2
	$\langle 100 \rangle$	$1 \div 3$	320	8
	$\langle 100 \rangle$	$4 \div 8$	320	8
Full Size	$\langle 100 \rangle$	$1 \div 3$	320	14
	$\langle 100 \rangle$	$4 \div 8$	320	10

Table 3: Bulk parameters of the multigeometry and full size 6" prototypes from Hamamatsu.

greater than 500 V). A percentage of bad strips less than 1 % is the usual requirement to maintain a reasonable overall efficiency per layer over the entire lifetime of the detectors.

Results on 6" devices discussed here are based on a set of 24 prototypes with a multigeometry design and 24 full size prototypes, both produced by Hamamatsu (see Table 3). A subset of the multigeometry devices were exposed to a fluence of 1.5×10^{14} 24 GeV protons/cm^2. The results from these tests are compared to the ones obtained for a set of 4" multigeometry detectors, also produced by Hamamatsu, irradiated up to a fluence of 4.0×10^{14} 24 GeV protons/cm^2. A detailed description of the results on the 4" prototypes can be found in [3]. The goal of these tests was to verify the suitability of large area sensors produced on 6" wafers, both for the inner and outer regions of the tracker. The dependence of the detector properties on the substrate thickness was studied on 6" multigeometry prototypes with $\langle 111 \rangle$ crystal orientation, as these were the only devices available from the producer in the short time scale scheduled for the tests. Results on detector parameters before irradiation are only marginally affected by the crystal orientation of the substrate although it is known that a larger dispersion of the values is present in the case of $\langle 111 \rangle$ devices when compared to $\langle 100 \rangle$ prototypes. On the contrary, after irradiation a significant increase in the interstrip capacitance is observed on detectors with $\langle 111 \rangle$ crystal lattice orientation, whereas no such effect is seen on $\langle 100 \rangle$ sensors [3] which have, therefore, been choosen. However, this does not affect the measurement of charge collection for the three thicknesses under test.

Multigeometry detectors have a surface of 62.5×62.5 mm^2, and consist of 12 sub–detector regions, each having 32 p^+ strips, independent bias and guard rings, and separated by n^+ implants. Four pitches are implemented (60, 80, 120 and 240 μm) with 3 different values of the width over pitch ratio (0.15, 0.20 and 0.30). Detectors are AC coupled and polysilicon biased, with the width of the metal strip being 8 μm wider (overhang) than the width of the p^+ implant.
Full size detectors have a surface of 109.5×82.5 mm^2 with 768 p^+ strips with 140 μm pitch and a sensitive length of 80 mm. Detectors are AC coupled and polysilicon biased, with the width of the metal strip being 12 μm wider than the width of the p^+ implant.

2.2 Comparisons between 6" and 4" prototypes

In Tables 4 and 5 the range of polysilicon resistors and the number of bad strips are compared for different batches of detectors produced on 4" and 6" lines. The spread of the values of the polysilicon resistors is comparable between the 4" and 6" detector samples and the fraction of bad strips (broken metal lines, broken coupling capacitors) in the case of the 6" production is well below the per mill level, an even better figure than for the 4" ones. This is an order of magnitude below the usual requirement of better than 1 %, and it demonstrates an excellent process quality.

Batch	GEOM1 $\langle 100 \rangle$	GEOM1 $\langle 111 \rangle$	GEOM2 $\langle 100 \rangle$	GEOM2 $\langle 111 \rangle$
N. of strips	1920	5760	4608	4608
	(384×5)	(384×15)	(384×12)	(384×12)
PolySi (kΩ)	1780-2210	1760-2080	1580-2200	1600-2450
Bad strips	none	2	4	3

Table 4: Parameters from Hamamatsu spec sheets of 4" multigeometry prototypes (see [3]).

Batch	Multigeometry					Full Size	
	$\langle 100 \rangle$ LR	$\langle 100 \rangle$ HR	$\langle 111 \rangle$ 320	$\langle 111 \rangle$ 375	$\langle 111 \rangle$ 410	$\langle 100 \rangle$ LR	$\langle 100 \rangle$ HR
N. of strips	3072	3072	1536	768	768	10752	7680
	(384×8)	(384×8)	(384×4)	(384×2)	(384×2)	(768×14)	(768×10)
PolySi (kΩ)	1770-2390	1800-2020	1810-2000	1880-2030	1880-2010	1860-2030	1860-2030
Bad strips	none	none	1	none	none	2	3

Table 5: Parameters from Hamamatsu spec sheets of 6" multigeometry and full size prototypes.

2.3 High voltage stability

Figure 4 shows the IV curves obtained from the Hamamatsu specification sheets of the full size 6" prototypes. Most devices show a total leakage current of less than 300 nA below 600 V, a remarkably low figure for such large devices and, once again, clearly indicative of an excellent process quality. Four of the devices show higher leakage currents, but only one displays clear micro-discharge behaviour below 600 V. All the detectors would be adequate for operation up to 400 V. These results have been cross-checked by our measurement on a sub-set of the detectors.

Figures 5 and 6 show the breakdown performance of the 4" and 6" series of multigeometry prototypes of 320 μm thickness, with the same substrate type, after the exposure to irradiation. All wafers are within specifications [1].

For $w/p > 0.2$ the high breakdown performance obtained on the 4" prototypes has been preserved in the 6" lines. This feature, which is known to be deeply process dependent, does not depend on

[1] In a subset of the 4" multigeometry prototypes, regions having the width of the metal readout strip narrower than the width of the p^+ implant were present. The significant improvement in the high voltage stability of the detectors when aluminium strips are wider than the implant is discussed extensively in [3].

a particular processing line.

The high voltage behaviour has been investigated after exposure to irradiation in the thicker detectors. Figure 7 shows the breakdown performance of $\langle 111 \rangle$ detectors of 410 μm thickness from the 6" multigeometry sample irradiated to 1.5×10^{14} p/cm^2. Breakdown voltages above 400 V are obtained for all the pitches in the overall range of w/p. Stable detectors operation up to 600 V is obtained for values $w/p \geq 0.2$ and for all the pitches up to 120 μm while the breakdown performance is degraded in the case $p = 240$ μm and $w/p < 0.2$.

2.4 Strip capacitances

The importance of the strip capacitance for the expected signal-to-noise ratio has been widely discussed in the TDR. In the case of the sensors for the outer tracker, the use of a different detector thickness requires a careful evaluation of this important parameter. The behaviour of the interstrip and backplane capacitance has been studied in detail for all possible pitches ranging from 60 to 240 μm in 300 μm thick devices. The outcome of this study is that there is a subtle interplay between interstrip and backplane capacitance so that the total capacitance is almost independent of the pitch and function only of the width over pitch ratio. This result leads to the expectation that the total capacitance is independent also of the thickness for pitches smaller than the thickness.

This study has now been extended to devices with thicknesses ranging from 320 to 410 μm. Figure 8 shows the results obtained from the measurements before irradiation of the interstrip and backplane capacitance in devices with a fixed value of $w/p = 0.15$ but different thickness. We observe a decrease of the backplane capacitance, which becomes smaller in thicker devices, compensated by an increase of the interstrip capacitance due to a stronger coupling to the neighbouring strips, thus confirming the expectations.

Figure 9 shows the total capacitance per unit length as a function of w/p measured in $\langle 111 \rangle$ 6" not irradiated multigeometry devices of three different thicknesses. The best fit lines for the three sets have similar parameters indicating that the relation $C_{tot}(\mathrm{pF/cm}) = 0.8 + 1.7 w/p$ can be assumed as a valid parametrization of the total strip capacitance per unit length, independent of the detector thickness.

Figure 10 shows the total capacitance per unit length of 4" and 6" devices with $\langle 100 \rangle$ crystal orientation before and after exposure to a fluence of 4.0×10^{14} and $1.5 \times 10^{14}\mathrm{cm}^{-2}$ 24 GeV proton respectively. In both the cases no changes in the capacitance are observed after irradiation, confirming that the processes on the 6" wafer production lines are of the same high quality as for the 4" ones.

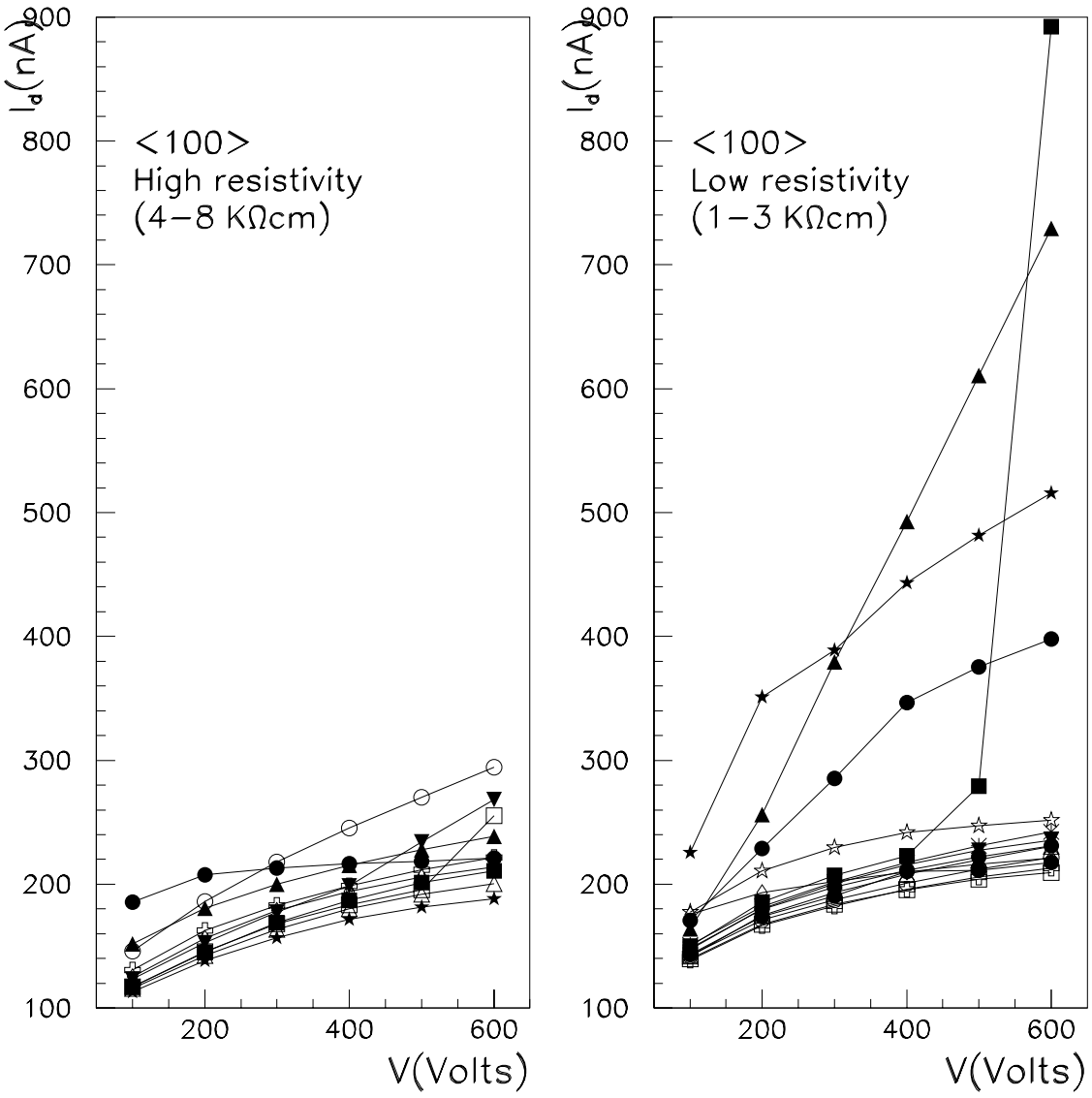

Figure 4: IV curves of the full size 6" devices (320 μm thick) as from Hamamatsu spec sheets. Measurements were performed at a temperature of 25 ± 1°C.

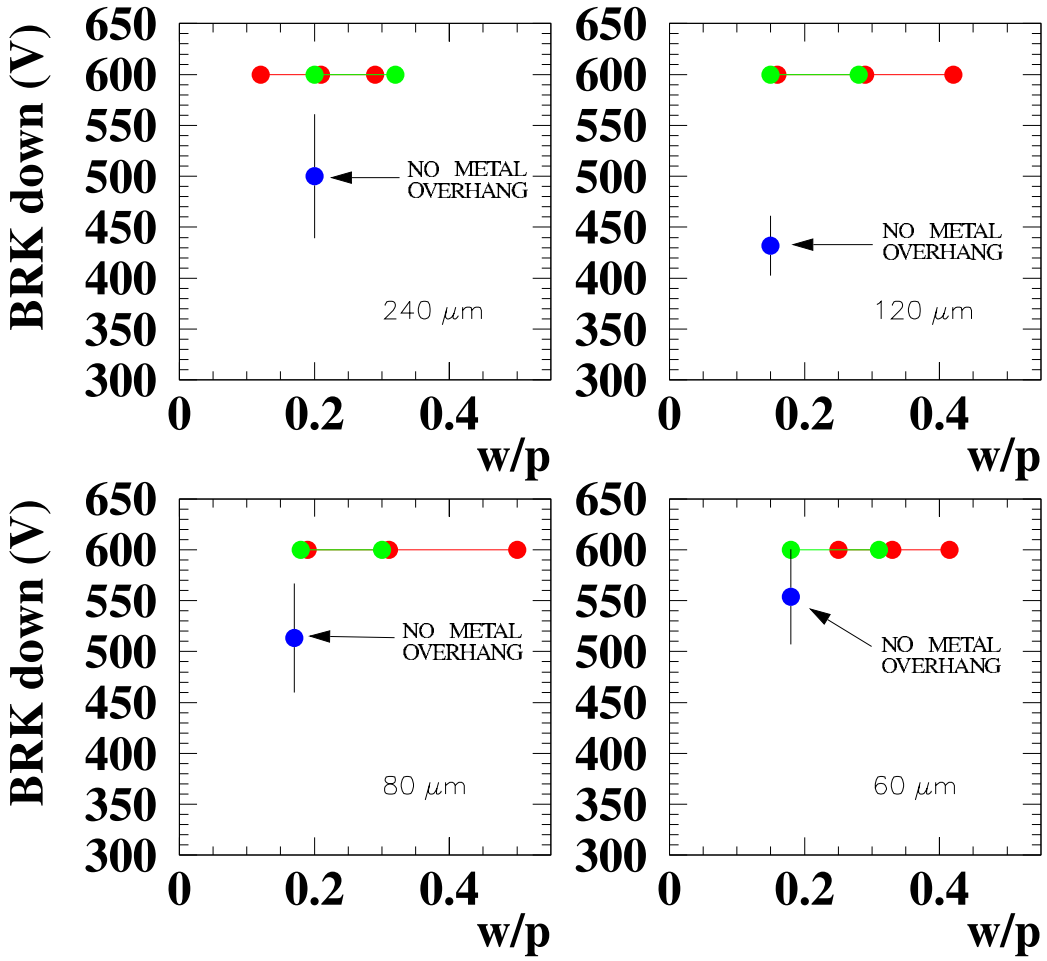

Figure 5: Breakdown voltage measured in ⟨100⟩ low resistivity 4" devices of 320 μm thickness after exposure to a fluence of 4.0×10^{14}cm^{-2} 24 GeV protons as a function of implant width over strip pitch. The strip pitch is indicated in each sub-figure. The black, single points represent regions with the width of metal readout strips narrower than the width of the p^+ implant. This layout was only present in the 4" multigeometry prototypes.

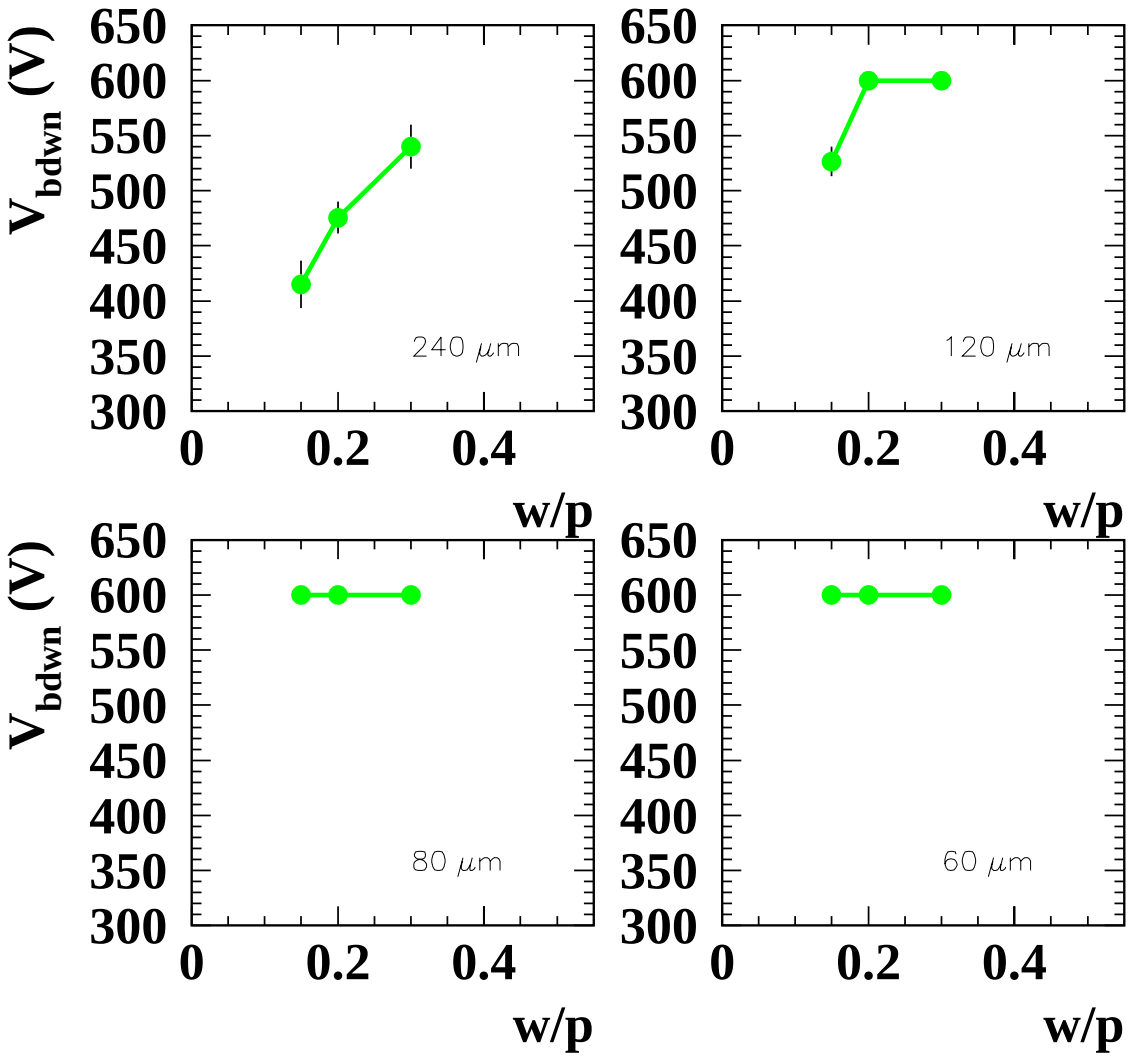

Figure 6: Breakdown voltage measured in $\langle 100 \rangle$ low resistivity 6" devices of 320 μm thickness after exposure to a fluence of $1.5 \times 10^{14} \mathrm{cm}^{-2}$ 24 GeV protons as a function of implant width over strip pitch. The strip pitch is indicated in each sub-figure.

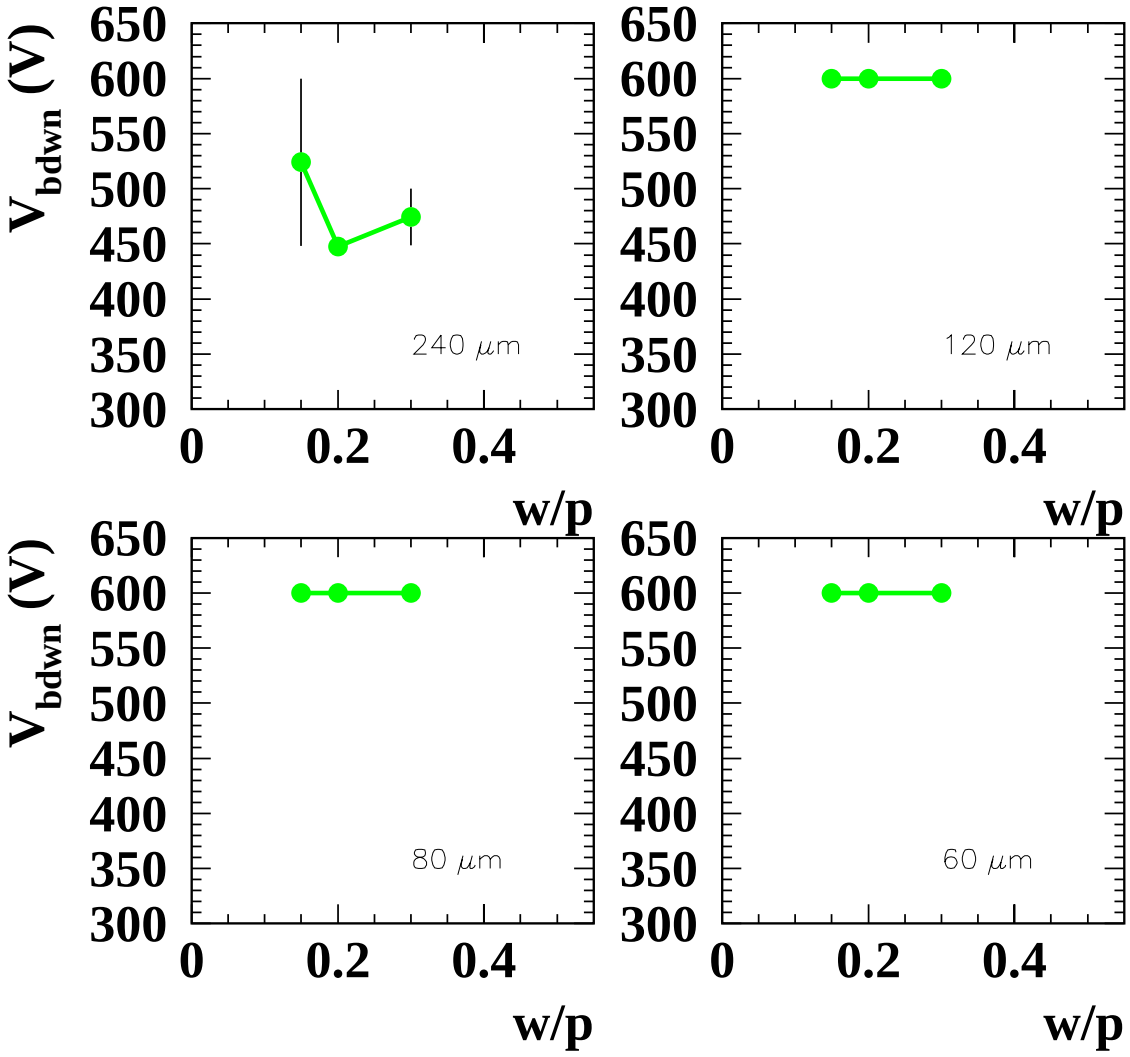

Figure 7: Breakdown voltage measured in $\langle 111 \rangle$ high resistivity 6" devices of 410 μm thickness after exposure to a fluence of 1.5×10^{14}cm^{-2} 24 GeV protons as a function of implant width over strip pitch. The strip pitch is indicated in each sub-figure.

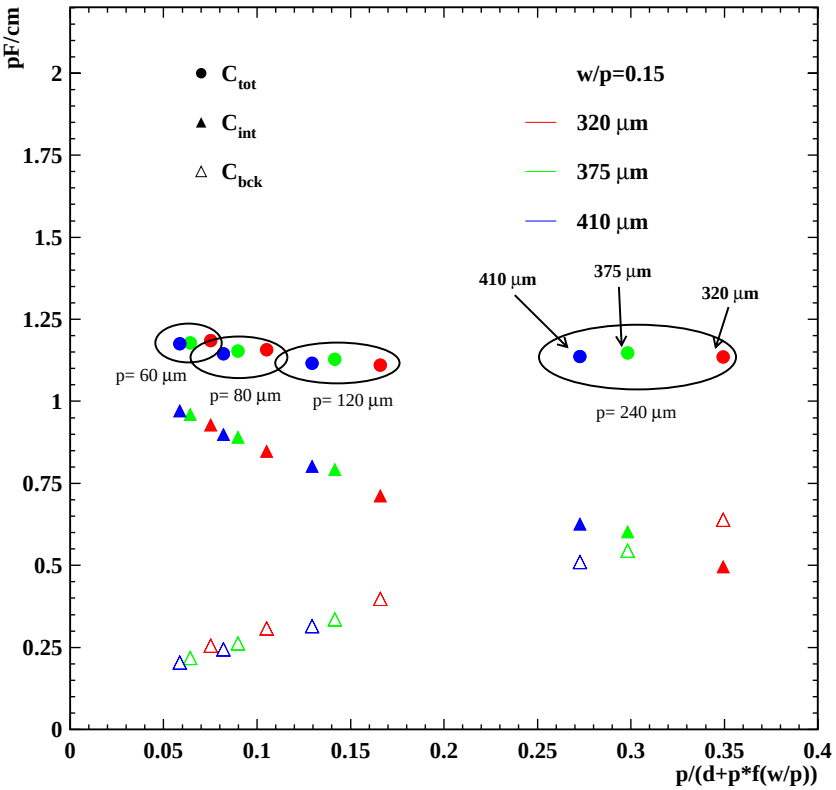

Figure 8: Backplane capacitance (C_{bck}), interstrip capacitance (C_{int}) and the sum of the two (C_{tot}) measured in ⟨111⟩ 6" not irradiated devices of three different thickness (d) but with the same value of the width over pitch ratio (w/p). Values are per unit length and expressed as a function of the parametrization (see [4]).

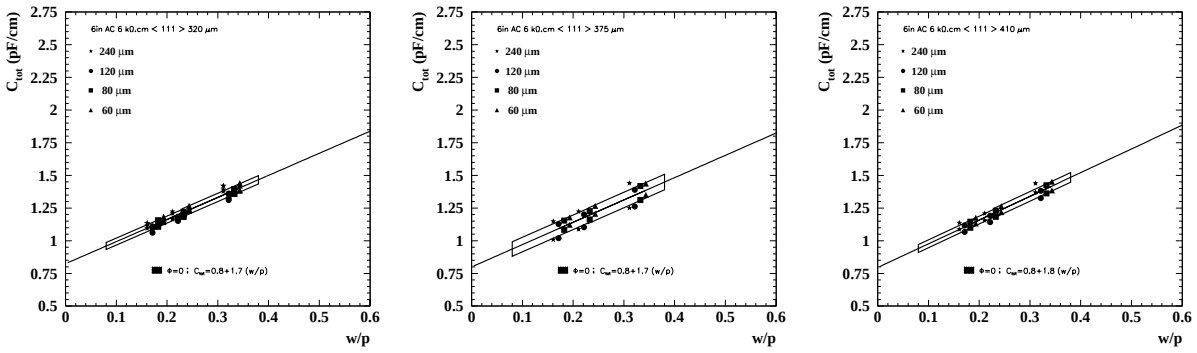

Figure 9: Total capacitance per unit length measured in ⟨111⟩ 6" multigeometry devices of three different thicknesses before exposure to radiation. Points represent different measurements while the band is the 1 standard deviation region for around the best line fit.

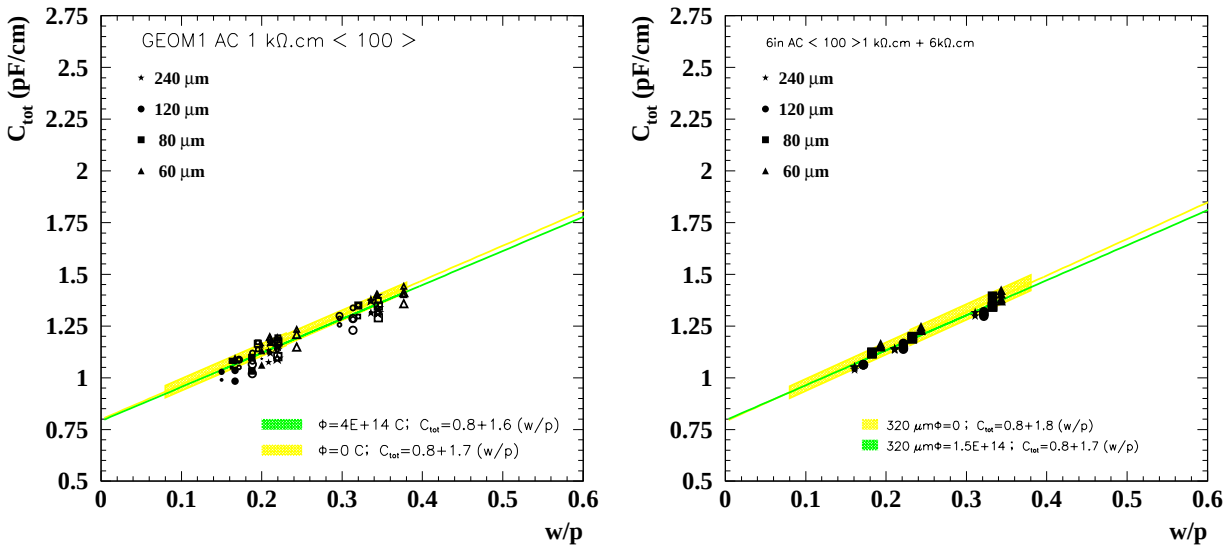

Figure 10: Total capacitance per unit length measured in $\langle 100 \rangle$ 4" devices (left) and $\langle 100 \rangle$ 6" devices (right) before and after an exposure to a fluence of $4.0 \times 10^{14}\mathrm{cm}^{-2}$ (4") or $1.5 \times 10^{14}\mathrm{cm}^{-2}$ 24 GeV protons (6"). The light grey band represents the one standard deviation region for not irradiated detectors around the best line fit; points represent different measurements after the irradiation.

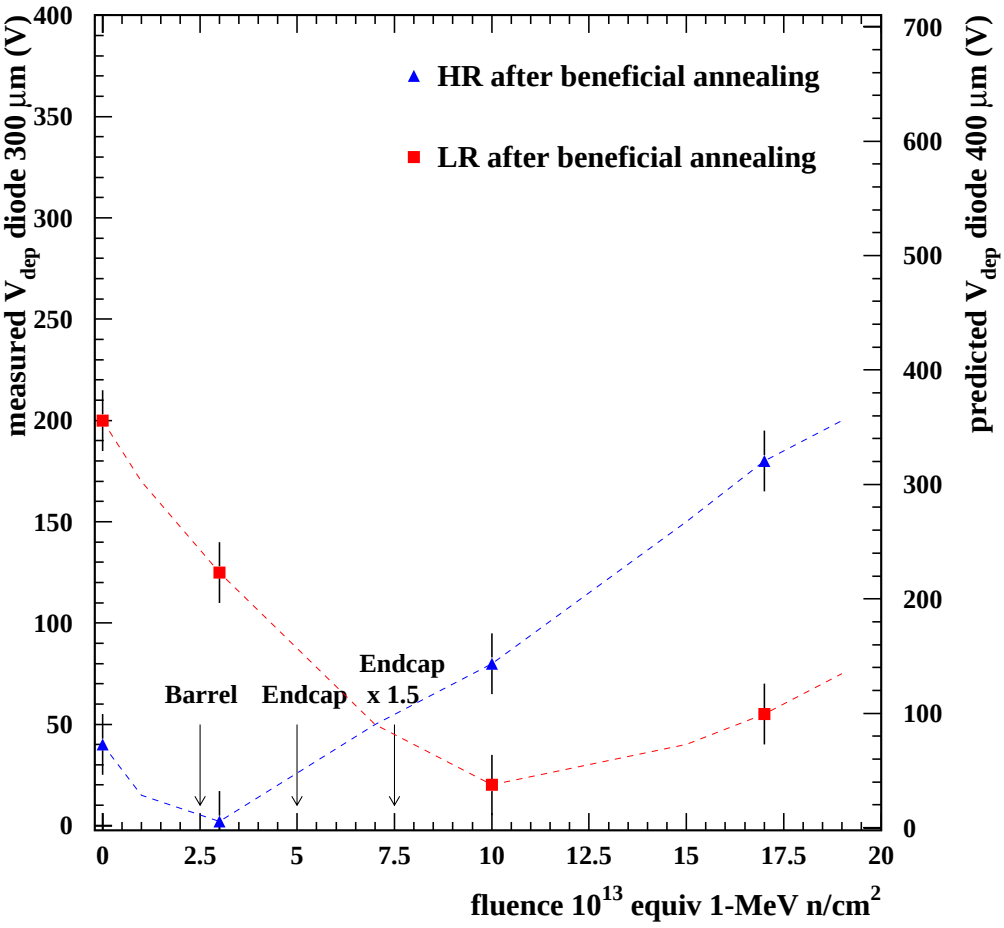

Figure 11: Measured depletion voltage for 300 μm thick diodes and extrapolated value to 400 μm thickness as a function of fluence in equivalent 1 MeV neutrons. The maximum fluences expected from the TDR for the barrel and endcap outer tracker are indicated. Lines are drawn to guide the eye.

2.5 Depletion voltage and charge collection efficiency

Figure 11 shows the depletion voltage measured on diodes of 300 μm thickness for 2 different initial substrate resistivities (**H**igh **R**esistivity and **L**ow **R**esistivity) as a function of the fluence in units of equivalent 1-MeV neutrons/cm^2. The values can be interpreted in terms of an effective charge carrier concentration and, hence, in the expected depletion voltage for 400 μm thick devices. In the range of fluences expected in the experiment, the detectors will operate always below or close to the point of type inversion. This implies that the voltage required to deplete the 400 μm thick devices will be low, always less than 150 V, independent of the choice of the initial substrate resistivity.
Figure 12 shows the measured charge collected from 6" $\langle 111 \rangle$ 5 kΩcm initial resistivity detectors irradiated up to 1.5×10^{14} p/cm^2 (see appendix A) with two different thicknesses, 320 μm and 410 μm (see Table 3). The operating voltage was set to 250 V and 400 V respectively after a voltage

scan performed to reach a plateau value in the collected charge. The charge collected in the 410 μm thick devices is actually 30 % larger than in the case of the 320 μm indicating that 400 V ensures a full charge collection in the thicker detector and that the collected charge scales indeed with the thickness.

This program of charge collection measurements is currently being extended to thicknesses of 500 μm and beyond. A wafer thickness of 500 μm is currently an industry standard for 6" lines and would simplify the production further. Prototypes (from ST-Microelectronics) are currently being prepared for irradiation. Results are expected in spring 2000.

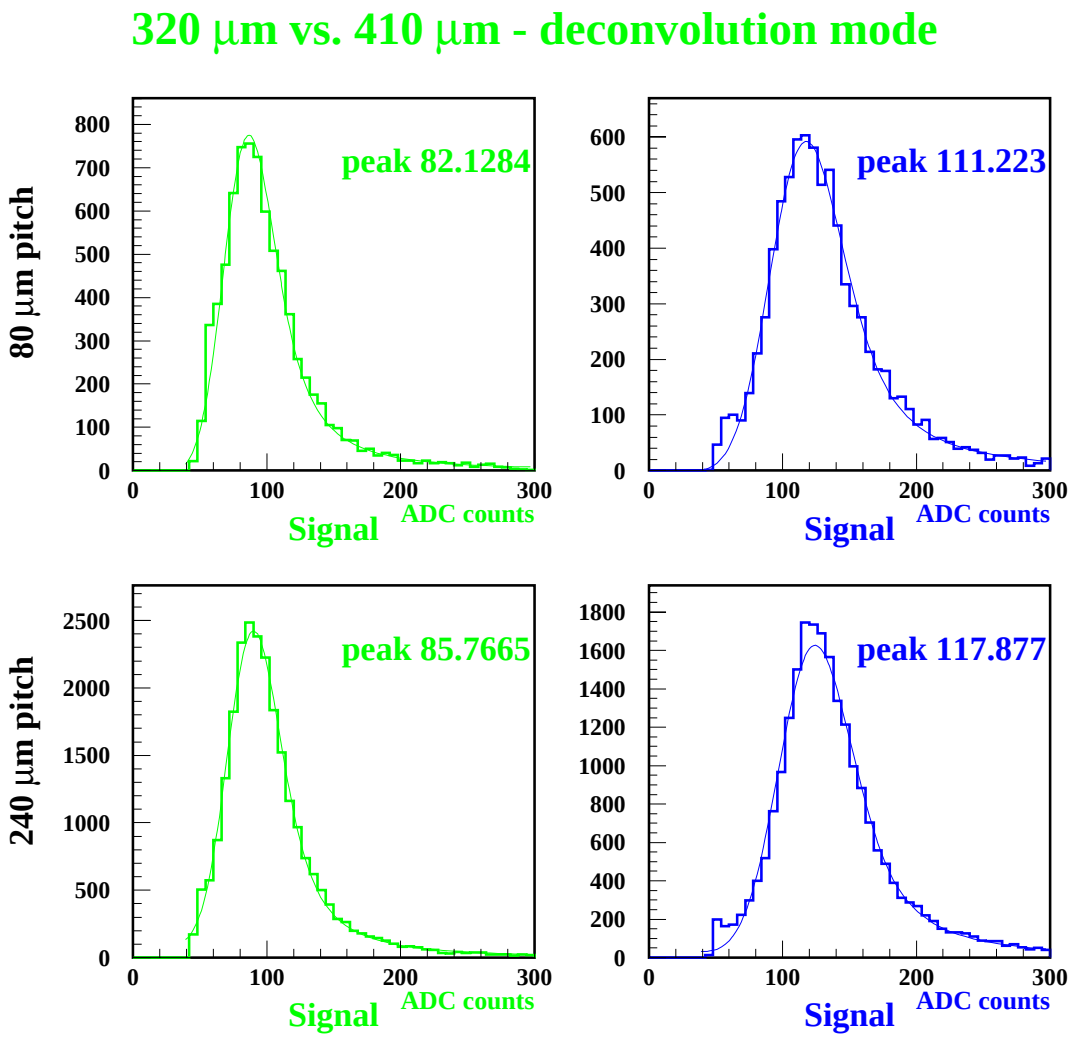

Figure 12: Signal measured on $\langle 111 \rangle$ high resistivity 6" devices of 320 μm (left) and 410 μm (right) thickness after exposure to a fluence of 1.5×10^{14}cm^{-2} 24 GeV protons for two different pitches.

3 Module read-out and expected Signal to Noise Performance

The read-out system for the CMS Tracker [1] is based on a 128 channel, pipelined analogue front-end chip (APV) with an analogue optical link carrying the signal to the digitizers in the counting rooms of the experiment. A "deconvolution" algorithm making use of analog signals sampled for three consecutive bunch crossings is incorporated into the APV chip, and provides rise and fall times very nearly equal to the 25ns bunch crossing interval.

The APV chip must operate for at least 10 years in the radiation field of the CMS Tracker, with little or no degradation in performance allowed. The APV has been successfully implemented in two radiation hard technologies (Harris and DMILL).

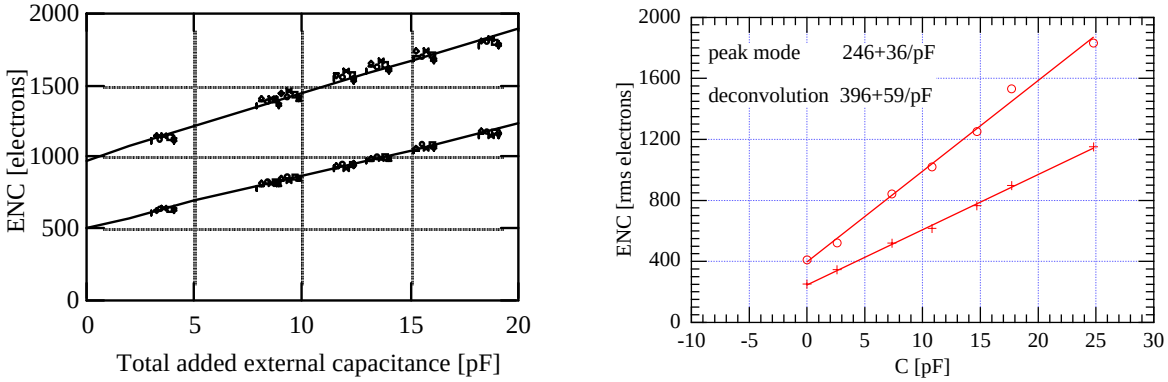

Figure 13: APV 6 (left) and APV 25 (right) noise performance as a function of the external capacitance in the deconvolution mode (top line) and in the peak mode (bottom line).

Based on the measured performance of these chips (Fig. 13), and of the rest of the analogue chain, a total electronic noise of 2000 e- is expected for the inner silicon tracker modules, in the deconvolution mode (see Table 6 for details of the noise calculation).

	noise contribution (e^-)	cumulative noise (e^-)
APV 6	1000 + 50 × 15 pF	1750
metal strip resistance (200 Ω)	500	1820
I_{leak} (1 μ A)	350	1850
optical link	600	1950
total		2000

Table 6: Breakdown of the noise contribution for detectors in the inner silicon using the APV 6 chip in deconvolution mode.

Assuming a most probable signal of 24'000 e- for a 300 μm thick sensor ($\sim$ one mip), and allowing for a 15 % loss of charge in irradiated silicon detectors, this results in an expected S/N ratio of approximately 10. Recent test-beam results with irradiated sensors read out by the APV chip are consistent with this expectation.

Procurement of the APV chip in specifically radiation hard technologies was one of the main cost driving elements of the CMS Tracker. Approximately a year and a half ago, a parallel program was initiated aimed at implementing the APV chip in 0.25 micron technology (APV25). The main motivation for this was the possibility of obtaining the required performance from a fully standard industrial process, by simple design rule modifications. This is expected to result in cost savings of approximately 10 % of the total cost of the Tracker. Furthermore, the input transistor performance in the 0.25 micron technology promised a significant reduction in electronic noise.

The first attempt at implementation of the full APV25 was a success, and resulted in a chip which already provides about a 20 % noise reduction with respect to the previous radiation hard versions (Fig. 13).

First radiation tests confirm that the pulse shape and gain are maintained after a 10 LHC year equivalent dose (see Fig. 14), as is the noise performance. Small flaws in the layout of this first prototype chip have since been identified and, by addressing them, a further decrease in noise is expected.

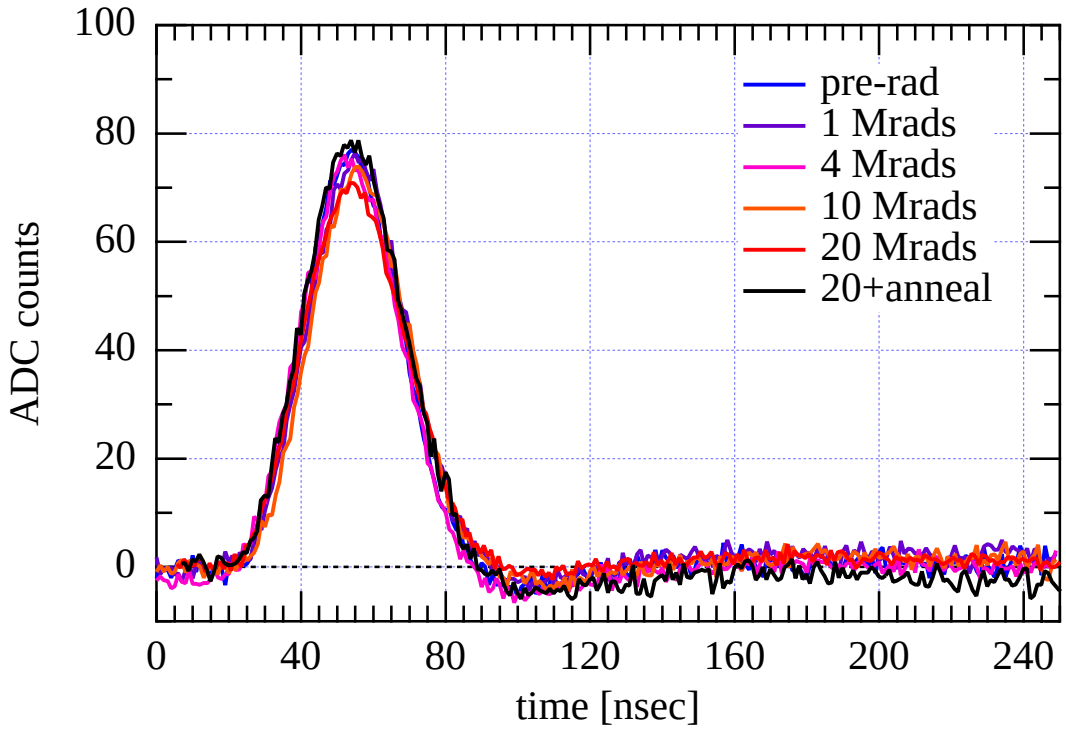

Figure 14: Time structure of the signal from the APV 25 chip after various irradiations, in deconvolution mode.

Based on the performance of the current APV25 chip, the total electronic noise expected for the inner silicon tracker is reduced to 1600 e- (see Table 7 for details of the noise calculation). The expected S/N ratio consequently increases to 13.

	noise contribution (e^-)	cumulative noise (e^-)
APV 25	400 + 60 × 15 pF	1300
metal strip resistance (200 Ω)	500	1390
I_{leak} (1 μ A)	350	1440
optical link	600	1560
total		< 1600

Table 7: Breakdown of the noise contribution for detectors in the inner silicon using the APV 25 chip in deconvolution mode.

When extrapolated to the outer silicon tracker modules with longer strips and thicker substrates, the resulting noise figure is of 1850 e- (see Table 8 for details of the noise calculation). Taking into account the increased signal collected with a 400 μm thick detector, this provides an expected S/N ratio of aproximately 15.

	noise contribution (e^-)	cumulative noise (e^-)
APV 25	400 + 60 × 20 pF	1600
metal strip resistance (200 Ω)	500	1680
I_{leak} (1 μ A)	350	1710
optical link	600	1810
total		< 1850

Table 8: Breakdown of the noise contribution for detectors in the outer silicon using the APV 25 chip in deconvolution mode.

4 Modules

4.1 Basic module layout

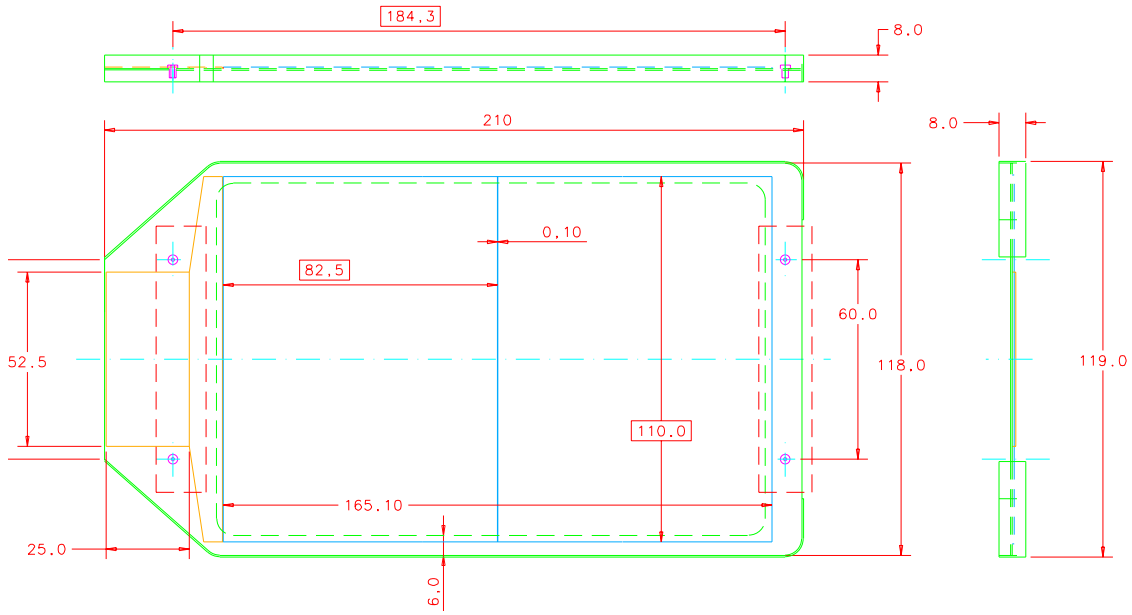

Figure 15: Barrel module for the outer tracker.

Fig. 15 shows the basic module layout for the outer barrel. The concept is similar to the one adopted for the inner tracker. A high conductivity carbon fiber (CF) frame holds two silicon detectors daisy chained and connected to a read-out hybrid via a pitch adaptor. Four positioning pins are used for fixation and alignment purposes. The active dimensions of a sensor are 110×165 cm^2: the overall dimensions of a module are 118×210 cm^2. Six front-end chips are used to read-out the 768 channels of the r-Φ view. The CF frame is in good thermal contact with cooled, high conductivity CF ledges which act as heat sinks. To increase the uniformity of the temperature distribution in silicon, the frame is in contact with the cooling system at both ends.

A similar solution is adopted for the outer end-cap modules. Here, three different geometries are required to match the three radial rings (see Fig. 3). Fig. 16 shows a draft design of the trapezoidal modules to be used for ring nb. 1 of the outer end-cap disks. The active dimensions are 104/126 $\times$ 158 cm^2 for the silicon sensors while the overall module dimension is 114/138 $\times$ 203 cm^2. All end-cap disks are identical. The same approach already used in the inner silicon tracker will be be adopted for double-sided modules both in the outer barrel and in the end-cap detector. Two pairs of sensors are coupled back-to-back on the same supporting frame, the second pair tilted by 100 mr with respect to the axis of the untilted pair.

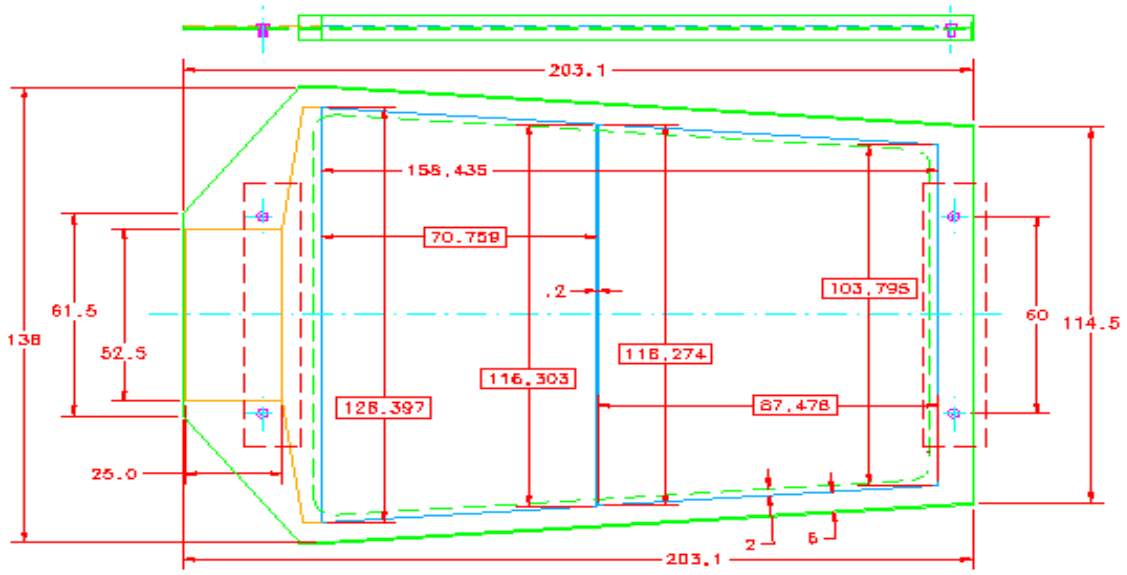

Figure 16: End-cap module for the outer tracker.

4.2 Modules assembly

The operation of module assembly is conceptually similar to the one adopted for the inner tracker. The basic steps consist of the assembly of a carbon fibre frame followed by glue application and then pick and place of components (sensors, hybrids). After glue curing the wirebonding of the strips to the readout electronics is done. Finally testing and, if necessary, repairs are performed. The wirebonding procedure is somewhat simplified with respect to the inner silicon tracker in that the larger sensor pitch means that in many cases a single row of bonds to the sensor can be made instead of the double row needed for small strip pitches. In all other aspects, the outer tracker module production is expected to be very similar to that for the inner tracker.

4.3 Automated procedures and preliminary results

Since the total number of modules is very large, we have developed automated procedures for module assembly and microbonding. Implementation of automated procedures will give a much higher throughput and will result in much reduced manpower requirement than for traditional manual techniques. It will also guarantee a higher reproducibility and better quality control of the modules. Because of these reasons, automated procedures will also be adopted for the production of inner tracker modules.

A total of 10,000 modules (for the outer tracker) have to be produced over a time of 2.5 years (500 working days).

Of the basic steps involved in module production (as described in the previous section), we have concentrated on two key time-consuming operations which would gain significantly with automation: the module assembly and the detector readout microbonding. For module assembly, we have undertaken a pilot project based on the use of a high precision robotic positioning machine. This set-up is shown in Figs. 17 and 18.

Figure 17: View of the test set-up of the automated assembly system.

A set of 4 modules can be prepared at a time. All components are first placed on the two work platforms (see Fig. 18). The components for one module consist of 2 silicon detectors, a pitch adaptor, a hybrid and and a CF frame. The machine dispenses glue onto the CF frames, then the components are placed in their nominal positions under the precise x-y-z-Φ control of the machine. The proper handling of the very delicate sensors during the pick and place operations is assured by means of flat teflon-coated vacuum pickup tools with built-in pressure sensors that prevent any large forces from being applied to the sensor surfaces. Once the components are positioned, vacuum valves are enabled which secure the detectors and the frames into place on the vacuum chucks under each of those components. The platform containing the 4 assembled modules can be removed for glue curing and another platform brought in to start the assembly of the next 4 modules. The time for assembling a set of 4 modules is about 30 minutes based on the module assembly tests

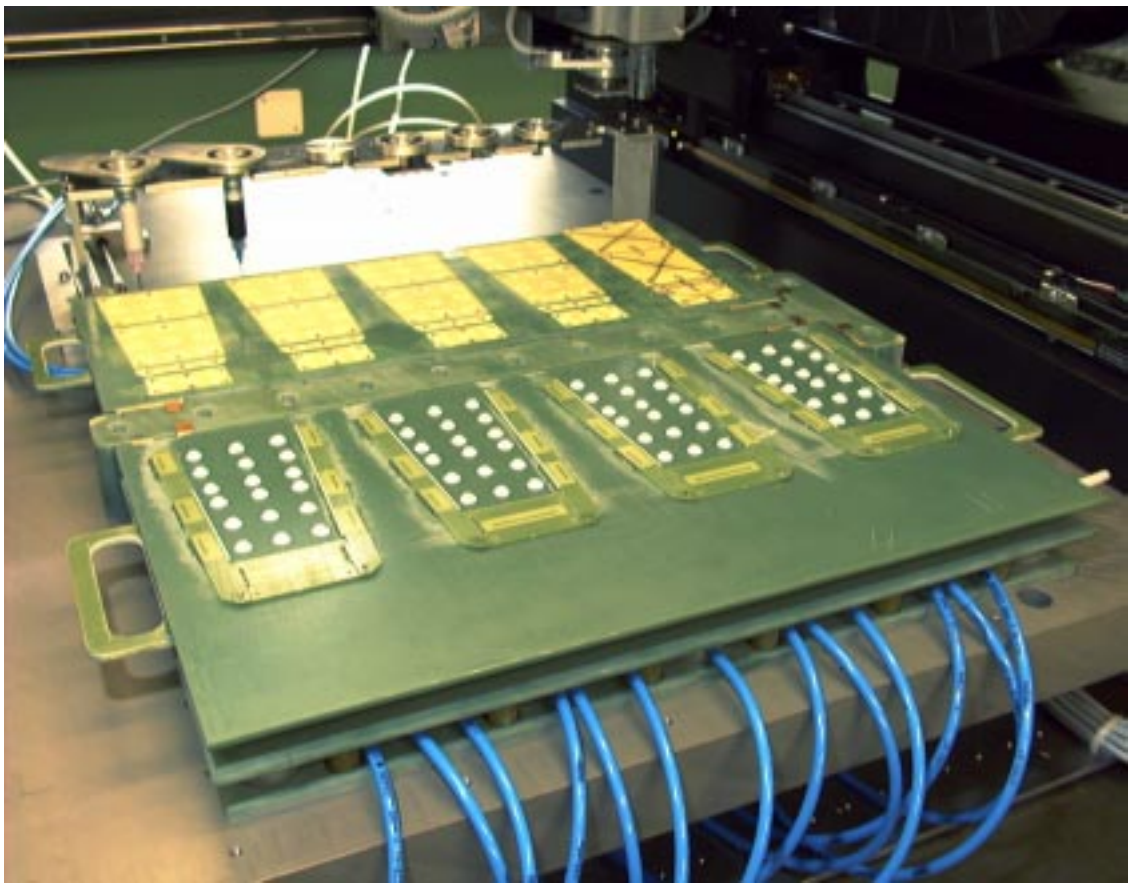

Figure 18: View of the assembly table with space for 4 end-cap detectors.

with the pilot project machine. This time includes conservative safety factors and allowance for maintenance and calibration of the equipment. The above production rate is based on the assembly of the smaller silicon modules of the inner tracker. The same set-up would be capable of handling 3 outer tracker modules at a time and hence the weekly throughput could be about 240 modules per week. The accuracy and reproducibility of the pick and place functions of the machine have been carefully evaluated. Fig. 19 shows results from the pilot project set-up. A reproducibility of better than 2 microns is obtained for a pick and place displacement in one coordinate. It is expected that an overall accuracy of placement of sensors of better than 5 microns should be obtained over the entire module surface for each module.

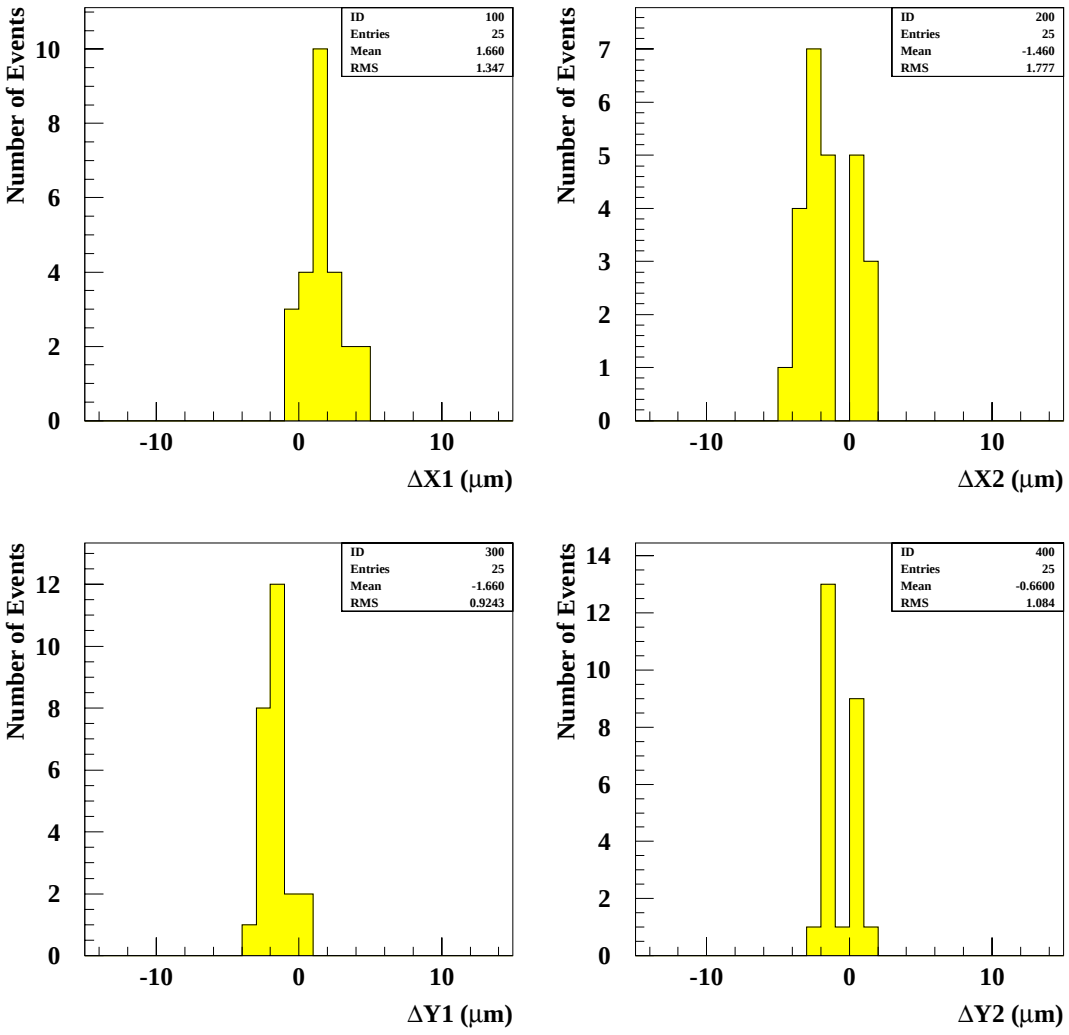

Figure 19: Precision obtained with the robot assembly machine for a pick and place sequence with a displacement in one coordinate using a silicon sensor. The x and y position placement errors for two points on each sensor are histogrammed for twenty pick and place trials.

In order to automate the microbonding operation, an automatic feed system has been constructed to

provide nearly non-stop operation of a semi-automatic programmable wire wedge bonding machine. Fig. 20 shows a test set-up.

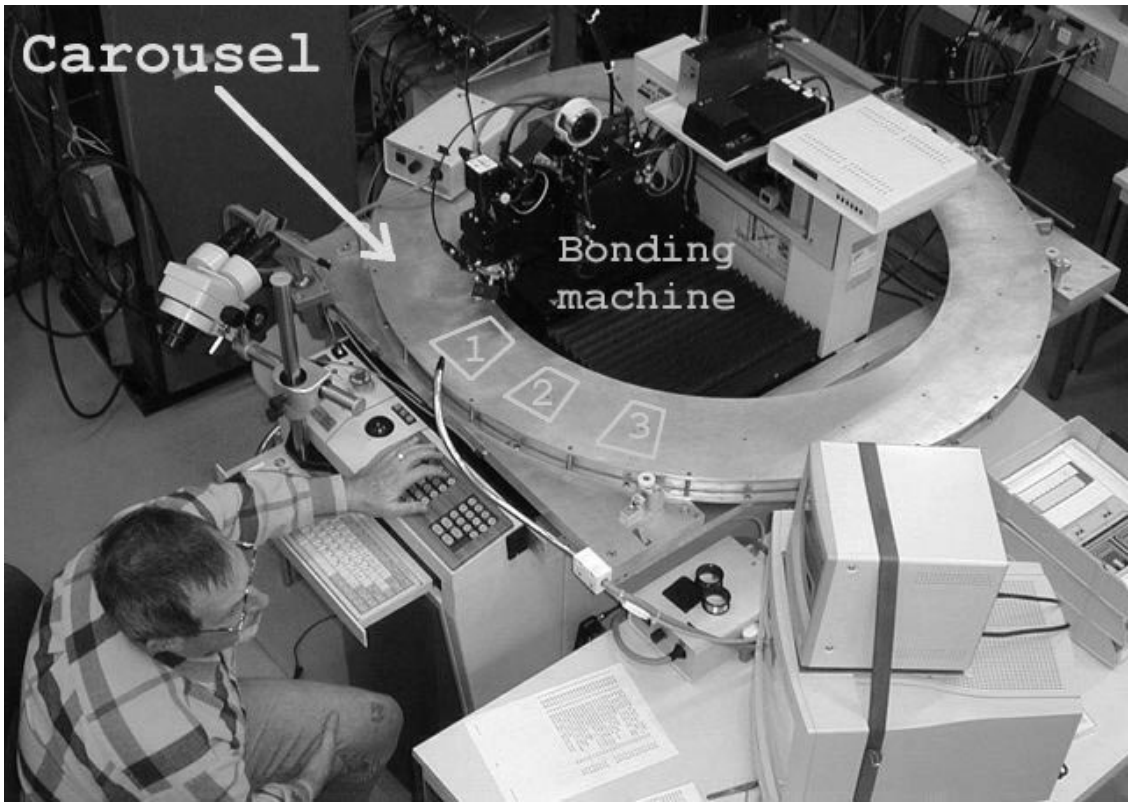

Figure 20: View of a test set-up showing the automatic feed system for the bonding machine.

A rotatable table ("carousel") is mounted on the bonding machine. This table is pneumatically driven under the command of the bonding machine so that when the bonding for one module has been completed, the machine can automatically index to the next module. Mounting of modules to be bonded and dismounting of completed modules can then take place even when the machine is bonding. A first carousel table has been constructed and is under test. The bonding machine considered as the baseline machine for the automatized module production is the Delvotec model 6400. Extensive tests with this machine have shown, when coupled to the carousel table, it should be capable of a throughput of 16 modules per day (a module is considered here to have 500 readout channels requiring 1500 wire bonds). This throughput includes set-up, error recovery and maintenance time as well as a reasonable safety factor.

A module readout test setup will be needed for each assembly centre so that as soon as a module is bonded it can be quickly (in 5-10 minutes) tested. This quick test is needed to identify any problems that are caused by the module assembly or bonding procedures so that such faults are not repeated in subsequent modules.

The automated module production schemes described above assume production of single-sided modules. Double-sided modules are assumed to be made of a single-sided r-phi type module mounted back-to-back with a single-sided stereo type module. In this scheme, no other special considerations are needed for stereo type modules (other than the minor tooling differences) compared to r-phi type modules.

4.4 Burn-in test and repair

A longer term burn-in test will also be needed in order to identify failures that may take longer to appear (infant mortality) or that might appear due to temperature cycling down to the minimum expected operating temperature of - 20 ^{o} C. It is envisaged that this test will last several days to one week. Because of this long duration the burn-in test will have to be done in parallel for a large number of modules. Because of the need for temperature cycling and the large number of modules involved, this test will require significant infrastructure such as a multiplexed DAQ system, multichannel power supply system, cooling and inert gas systems, and sophisticated monitoring and safety systems.

For modules that do not pass the acceptance criteria a repair has to be foreseen. Since the nature of the necessary repair may involve any aspect of a module (mechanical, electrical or electronic), the laboratories doing repair work must be well equipped: A probe station, high quality microscopes, bonding machine, measuring devices, and a full single-module readout test system would be required. The manpower requirement for this task will be physicists or highly trained technicians.

5 Mechanics, services and installation

The design of the mechanics for the all-silicon tracker relies on making extensive use of the studies performed so far for both the inner silicon and the outer MSGC tracker. In particular, we are currently evaluating full-scale prototypes of an inner barrel layer (Fig. 21), an inner forward disk (Fig. 22), an outer barrel wheel (Fig. 23) and outer forward disks (Fig. 24).

In contrast to the TDR tracker, the full silicon tracker requires a thermal screen at the outer radius of the tracking volume. The technology for this screen is the same as described in the TDR with additional developments described in [5].

Operating both the inner and the outer tracker at the same temperature opens the possibility of supporting the whole structure from an external support tube. In addition, one may consider the possibility of having end-cap disks in one piece, removing the radial gap in the end-cap, through which all cables and services for the inner tracker are routed. Compare Fig. 1 and Fig. 2.

5.1 Support structure

The MSGC barrel is already designed to be supported by an external support tube. Only minor modifications to the MSGC barrel structure are required in order to use the outer silicon detector modules (see Fig. 15). The length of the barrel is 13 silicon modules, carried by rods of 6 and 7 modules (see Fig. 25 for a rod with 7 modules). The rods are carried by the wheel, which has a design similar to the one described in the TDR, but with a number of layers reduced from 6 to 5. The rod openings are adapted to the dimensions of the silicon support rods (see Fig. 26).

The main characteristics of the module and rod mechanics with silicon detectors are summarized in Tables 9 and 10.

The MSGC endcap disks are also convenient structural elements to support silicon modules. The MSGC and the Silicon endcap both utilise a carbon fibre honeycomb sandwich disk as the primary support for the modules. There is no principal problem to support Si modules on the MSGC disk and many details of the inner Si endcap can be applied in the outer part of the endcap.

Figure 21: View of a prototype support structure for the inner barrel, some dummy silicon modules are mounted.

Figure 22: View of a prototype support structure for an inner forward disk, one dummy silicon module is mounted.

Figure 23: View of a prototype support structure for the outer barrel.

Figure 24: Prototype support structure for the outer forward disks.

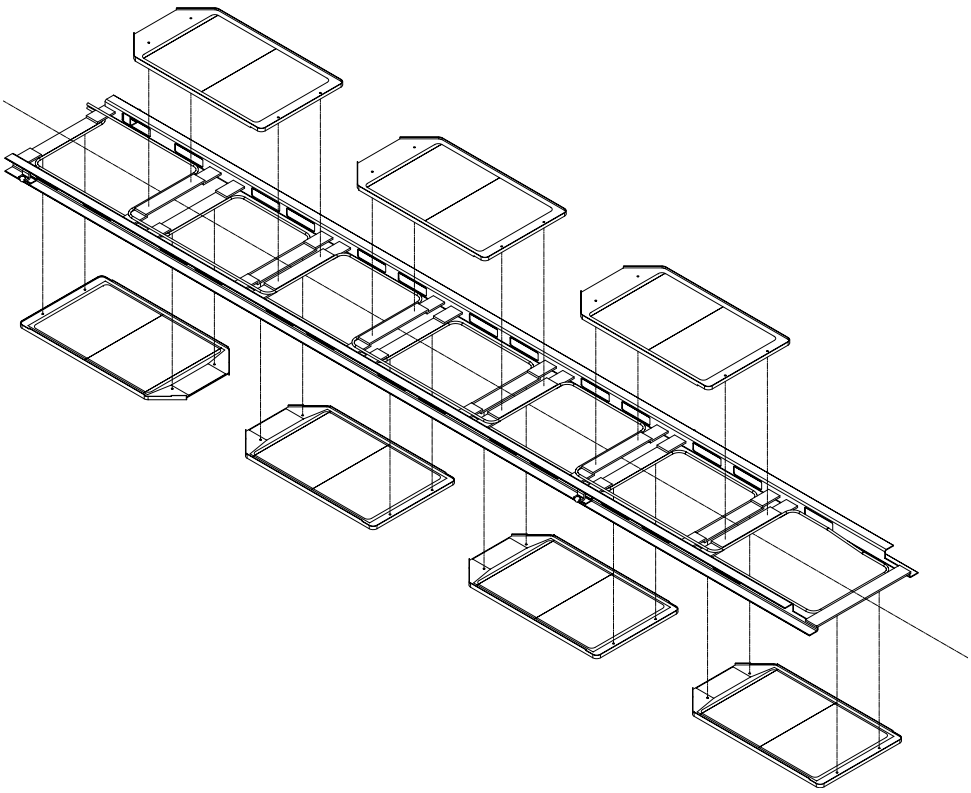

Figure 25: Rods containing either 6 or 7 modules each.

Module type	**Outer Silicon**	**MSGC (as reference)**
Active width	110 mm	122.88 mm
Active length	165 mm	250 or 125 mm
Read-out electronics	At one end of a module	At one or two ends of a module depending on module type
Double-sided modules	Two separate modules mounted back to back	Two separate modules mounted back to back
High-voltage	No	Yes
Gas	No	Yes
Operating temperature	$-10°$C	$+18°$C
Cooling	At both ends of the module Silicon detectors to be kept cold and remove heat from electronics and silicon detectors (leakage current). Carbon-fibre ribs around the module for improved heat removal.	At the corners of the module Remove heat from electronics.
Preferred Lorentz angle	$10 - 12°$	$14°$

Table 9: The main characteristics of the module mechanics.

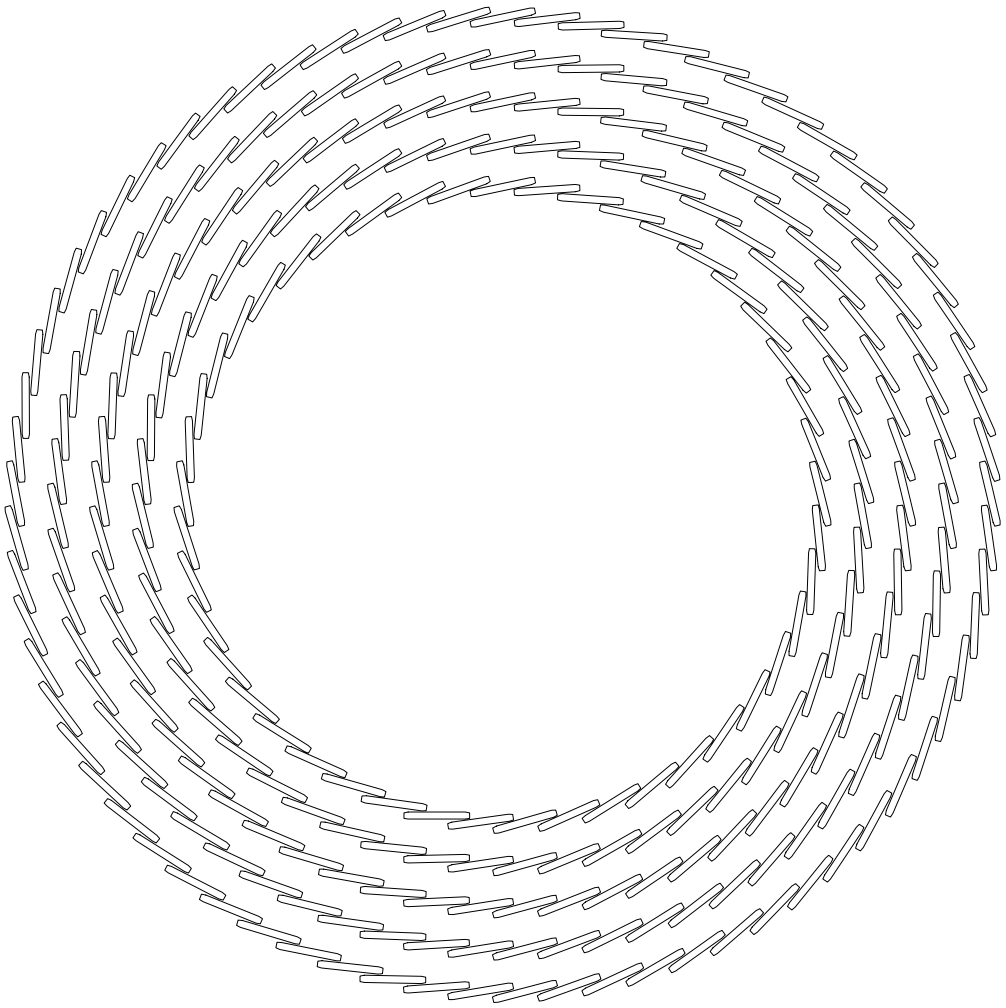

Figure 26: R-ϕ view of the barrel showing the distribution of rods.

Rod type	**Outer Silicon**	**MSGC (as reference)**
Rod support frame	Same as in MSGC. Dimensions modified for different module dimensions	
Number of modules	6 or 7	4.5
Cooling	2 mm diam. stainless steel tube running in zig-zag under the module electronics. It has a maximum total length of 2.3 times more than with the original MSGC.	2 mm diam. stainless steel running at the sides of the rod.
Low-voltage powering and read-out	As in MSGC	
Gas and high-voltage	No	Yes

Table 10: The main characteristics of the rod.

5.2 Cooling and services

The outer all-silicon tracker has the same number of electronics channels as the outer MSGC tracker and the silicon modules use very nearly the same front-end electronics as the MSGC modules. Therefore, the expected power consumption of the two systems is similar.

Cooling The cooling of a silicon module is an important engineering task and is described, for the inner modules, in the TDR. The same solution can also be applied to the outer modules. Continuous design, calculation and testing is on-going. At present the design work is concentrated at the level of the detector modules and the coupling of the cooling pipes. Large-scale tests have been started on the mechanical structures prepared for the milestones. However, no particular impact on the overall design of these support structures is expected.

Since the power dissipated in the bulk silicon is less than 10% of the power dissipated by a module, the total power to be removed remains the same as in the TDR layout. All external pipe-work, pumps and other installations are not modified with the exception of the refrigeration unit. More power is needed in the refrigerator since the operating temperature of the outer modules is now $-10°C$ compared to $+18°C$.

The end-flange layout remains as described in the TDR. The warm-cold feed- through of the large amount of cables in the limited space does indeed pose a significant challenge. We have designed and manufactured a first prototype. Testing will start soon. When a good understanding of the feed-through is reached, we will be able to design the optimal dry nitrogen flushing system. It is currently unclear whether a slight overpressure or under-pressure is optimal.

In general, no problem is expected in operating all mechanical structures at $-10°C$ since they are manufactured using low expansion materials.

Risk analysis and safety According to the current estimates, the silicon detectors will run at $-10°C$ with the cooling liquid at about $-20°C$. Since the module materials have low thermal expansion coefficients, the rapid cool down during a power failure will not damage the module. When the cooling fails with power on, the module temperature is estimated to rise about $5°C$ per minute. A protection system will be installed to switch off the power at a certain threshold temperature. This system will be hard hardwired and fully automatic, with exceptional reliability and without an override option.

Service space The space needed for the full silicon tracker services is similar to the space needed for the TDR layout services and no additional problems are to be expected.

The cooling pipes of the MSGC system were not insulated. Changing to silicon therefore requires the addition of insulating materials. Since the HV cables in the MSGC layout used a significant volume, the total space used by both systems is about equal. With the cold volume now extending to the outer radius and the cables also coming out at this radius, it is necessary to realise a warm-cold cable feed- through in a very confined space. Although a detailed design has to be carried out the feasibility is not under question. The increase of the services for the larger area thermal screen is negligible.

Dry gas distribution As mentioned above, a crucial item is the warm-cold feed-through. Absolute tightness is unachievable. Depending on the leak rate and the pressure difference a certain amount of cold air will enter the inter-detector space or warm air will enter the silicon volume. The cold air might have undesirable effects on neighbouring detectors and/or the warm and humid air will form ice inside the silicon volume. This problem needs to be solved, regardless of the quantity of silicon that will be used. An engineering effort is on-going.

5.3 Detector assembly, installation and maintenance scenario

The procedure for the assembly of the tracker and for its installation and maintenance depend on the layout. In the case we remain with a separated inner and outer tracker, as shown Fig. 1, a procedure similar to that described in the TDR can be used. This scenario is described below. The possibility of a different layout, similar to the one described in Fig. 2 is currently evaluated. The simplification of the maintenance scenario is one of the main criteria in choosing the layout.

A possible procedure for the tracker assembly and installation is explained in chapter 6.7 of the TDR. This procedure is still valid. During the time elapsed since the TDR the tracker community has studied in depth and modelled the assembly procedure. This has led to a more refined and significantly better understood sequence of assembly steps.

The outer Silicon subunits (barrel and the 2 endcaps) will be mounted onto the central support tube which is temporarily cantilevered from the inside. The thermal screen is installed on the outer radius integrated into the services supports. After the load transfer to the outer support brackets the cantilever will be removed. Then the inner Silicon barrel including the mini endcaps will be installed. The 2 inner Silicon endcaps will be moved in from both ends. Extensive tests and survey will be executed after each step. After preparation for the transport the tracker will be installed inside CMS. The full assembly and installation scenario is illustrated in a 25 step sequence [6].

The maintenance scenario as described in the TDR chapter 6 is still valid. We distinguish between short time access (allows access to racks located in the experimental cavern (UXC 55)), intermediate time access (allows opening of CMS endcaps, access to tracker patch panels and endflanges) and the end of year shut-down access.

A complete removal of the tracker from the beam line is not foreseen during the long shut down. A complete disassembly every year is unreasonable as long as the amount of damage is below a certain limit, typically a few percent of non working channels. In case of serious damage the tracker needs to be repaired. In this case a complete removal / installation during a somewhat extended shutdown is foreseen, however this will require a very substantial amount of trained manpower. The extraction of the tracker is feasible from the mechanical point of view, however the real difficulty is the disconnection and handling of the very large number of cables and service lines during the operation.

Since the total number of service lines for the TDR tracker and the full silicon tracker is about the same this procedure is similar for the all-silicon option. For the full silicon tracker a larger cold storage area in building SX than foreseen in the TDR will be reserved.

6 Performance

6.1 Introduction

We address in this chapter a preliminary evaluation of the performance of an all-silicon detector. The time-scale of this work and the resources available to do it have limited the desirable level of investigation and have led the authors to focus the study on some selected topics that we believe to be of the highest priority. Following this criterion, we report a comparison of the performance of the all-silicon layout discussed in this document with the tracker layout presented in The CMS Tracker Project Technical Design Report (TDR) [1].

6.2 Software

The software tools used to produce the results presented in this chapter have been described in [1], chapters 7 and 8. Some additional tools have been developed since the submission of this document which have also been exploited for these studies. To transport particles through the detector we still use the CMSIM simulation software [7], based on the GEANT package [8]. A large fraction of the existing FORTRAN digitisation and reconstruction algorithms used in [1] has nevertheless been re-formulated in C^{++} object-oriented code [11]. In the new digitisation software, some improvements have been introduced aiming to a better modelling of the signal readout. In the following, we report studies obtained by using both the FORTRAN and C^{++} software. A careful comparison of the two packages has been performed and equivalent performance has been required as a validation criterion. Indeed, we will specify the code source only when necessary, i.e. to refer to different digitisation algorithms.

6.3 Detector Layout

The geometry of the all-silicon Tracker (AST) layout has been modelled in CMSIM, at the same level of accuracy implemented to describe the tracker layout studied in the TDR (MST). Views of the AST outer barrel and end-caps are shown in Figs 27 and 28. A cut view of the AST layout is shown in Fig 29 and an equivalent picture of MST is shown in Fig 30. Some layers are instrumented with back-to-back sensors to provide space point measurement, as explained in the figure captions. In the following we will refer to these layers as "double sided". The two layouts differ in several aspects, as can be noticed by comparing the two figures

- MST has one more outer barrel layer, double-sided.
- The two double-sided layers of the outer AST barrel are set at the innermost radii

- The AST and MST outer barrel have different z-segmentation
- MST has two more disks in each end-cap
- The AST outer end-cap stations have one double-sided ring, the MST stations have two.
- The AST end-caps have less radial segmentation, i.e. three rings instead of four.

The outer tracker sensors in the AST layout are taken to be 500 μm thick. In the AST layouts, sensors in the inner and outer barrels are tilted to compensate for the Lorentz effect by 9 and 12 degrees respectively. In the MST layout inner and outer barrel sensors are tilted in opposite directions, due to the different charge of the carriers. The sensor tilt in the MST outer barrel is 14 degrees. The smaller tilt angle in the outer AST barrel is due to a compromise between the actual drift angle and the constraint posed by the existing mechanics. The thermal screen, decoupling the thermal conditions of the inner silicon and MSGC detectors has been positioned at the outermost tracker radius in the AST layout. The tracker support structures are unaltered as well as the service layout.

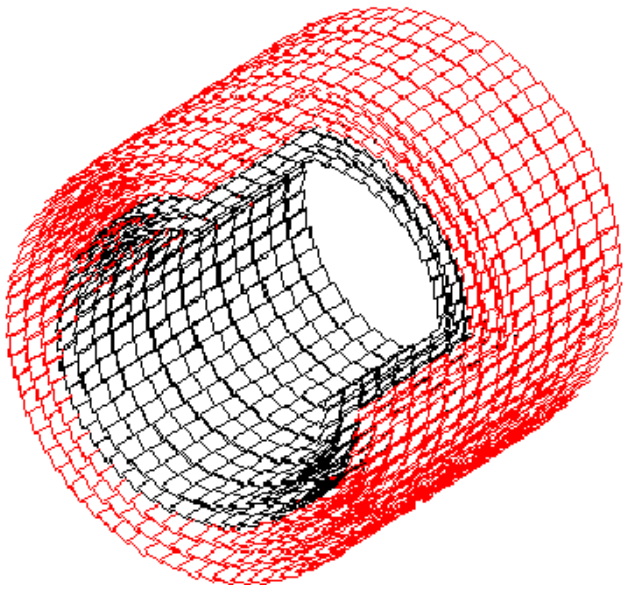

Figure 27: Outer barrel section of the all-silicon tracker layout as modelled in the Monte Carlo. The two innermost layers are equipped with sensors mounted back-to-back to provide space point measurements.

6.4 Tracker Material Budget

To evaluate the material budget of the AST detector some modelling assumptions were necessary. The AST outer barrel mechanics has been kept identical to the one of the MSGC barrel. The

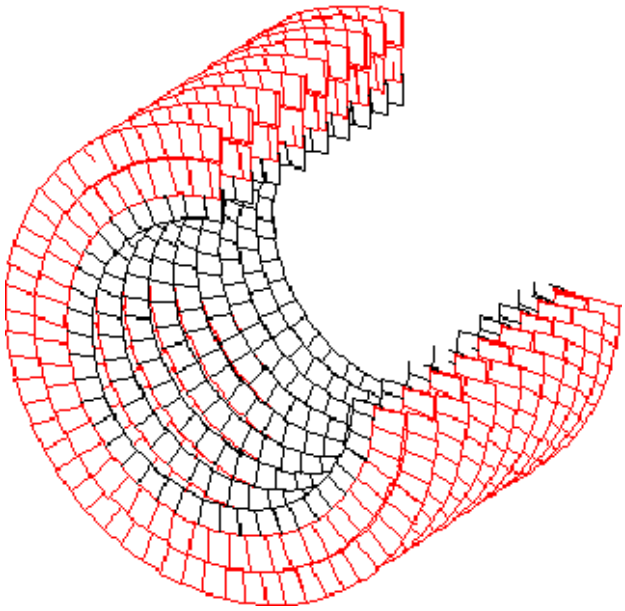

Figure 28: Outer endcap stations of the all-silicon tracker layout as modelled in the Monte Carlo. The innermost ring in each station is equipped with back-to-back sensors.

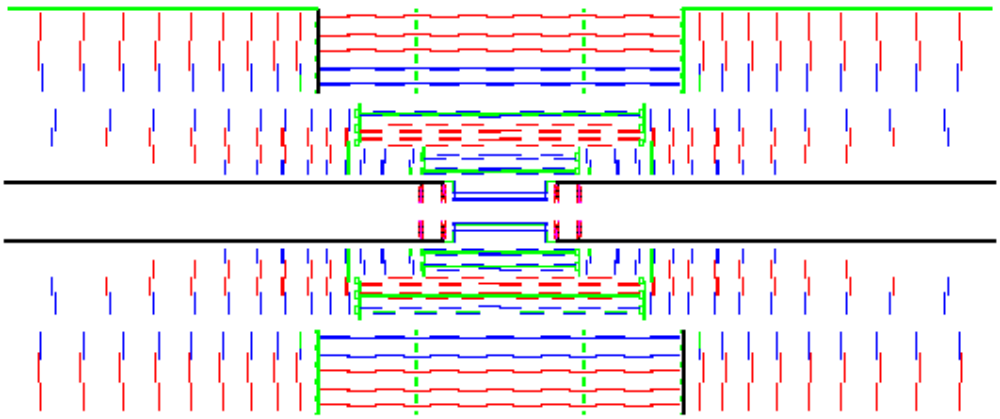

Figure 29: Longitudinal section of the all-silicon tracker layout as modelled in the Monte Carlo.

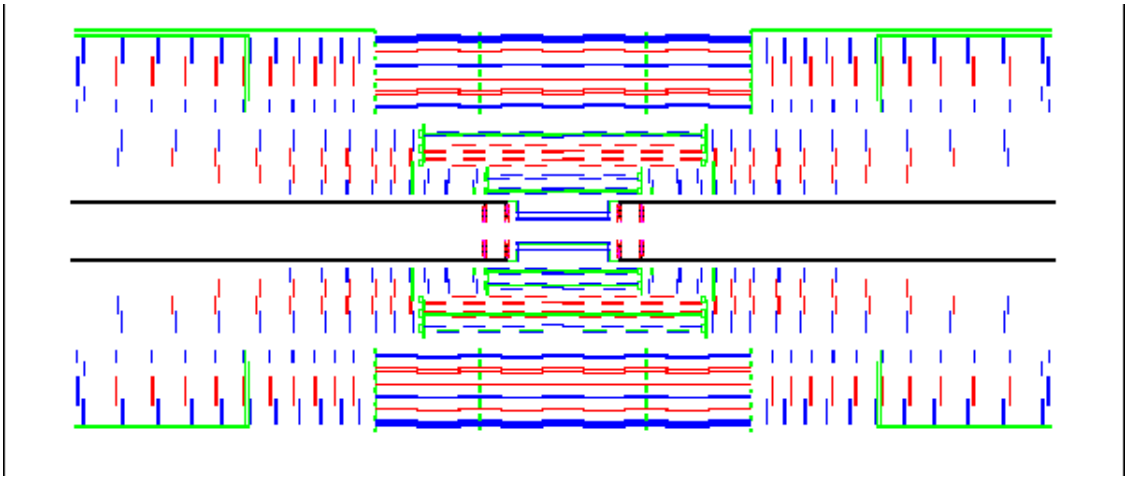

Figure 30: Longitudinal section of the silicon-MSGC tracker layout as modelled in the Monte Carlo. The first (innermost), fourth and sixth outer barrel layers measure space points. In the end-caps, all innermost and outermost rings are equipped with back-to-back detectors.

AST end-cap mechanics has been modelled by extrapolating the disk structure of the inner silicon end-caps. The weight of the extrapolated mechanics and of the MSGC disks are estimated to be comparable. The thermal screen has not been altered but for the radial position. The module mechanics for the outer AST sensors has been evaluated by engineers and reproduced in the Monte Carlo. The weight of a barrel sensor space-frame is $\simeq 8.9$ g to be compared to $\simeq 2.6$ g for the inner sensor structure.
The cooling inlets and outlets of the AST outer detector are the same as for MST. Nevertheless the cooling distribution inside the detectors has been modified. In the barrel, the actual pipe length has been increased by a factor 2.3, provisionally deemed necessary to meet the more severe cooling requirements specified for silicon detectors. This model could turn out to be conservative in light of further studies. For the outer AST end-caps, the cooling distribution model of the inner end-caps has been implemented. Other services and the read-out have been modelled consistently with what described in [1]. Major changes include the suppression of the high-voltage hybrids supplying the MSGC drift planes, a consistent rescaling of high voltage cables and the inclusion of thermal sensors throughout the detector. The same low voltage hybrid size is used in all AST sensors, while the MSGC hybrids used to be larger than the silicon ones. A comparison of the two simulated layouts in terms of hybrids, read-out channels and active surface is shown in Table 11. The electronic channels of the MSGCs have been counted taking into account an increase of pitch of 20% with respect to the layout discussed in [1].

The material contributed by the detector is estimated in units of radiation length, following the procedure described in [1]. The fractional radiation length contributed by the individual Pixel and Inner Silicon detectors is shown in Figs. 31 and 32 respectively. The contributions of the Outer

	Outer Silicon	MSGC	Inner Silicon	Total
Hybrids $[10^3]$				
AST			9.0	17.7
Barrel	4.9	6.6×2		
Endcaps	3.8	7.3×2		
MST			9.0	$23(LV) + 14(HV)$
Channels $[10^6]$				
AST			5.3	11.4
Barrel	3.4	2.8		
Endcaps	2.7	3.1		
MST			5.3	11.2
Surface $[m^2]$				
AST			64	214
Barrel	90	130		
Endcaps	60	88		
MST			64	282

Table 11: A comparison between All-Silicon and MSGC-Silicon layouts, as modelled in the Monte Carlo. Low and high voltage hybrids are reported separately for the MSGC detector.

Silicon and MSGC detectors are shown in Figs. 33 and 34, while the ratio of the two histograms is shown in Fig. 35. Fluctuation in the histogram showing the ratio are dominated by the different position of material such as hybrids, cooling pipes and disks in the two layouts. In the barrel region, the two detectors show a comparable material budget, the Outer Silicon barrel being just slightly higher at large $|\eta|$. The AST outer end-caps are clearly lighter than the MSGC end-caps, due to the smaller number of stations and rings.

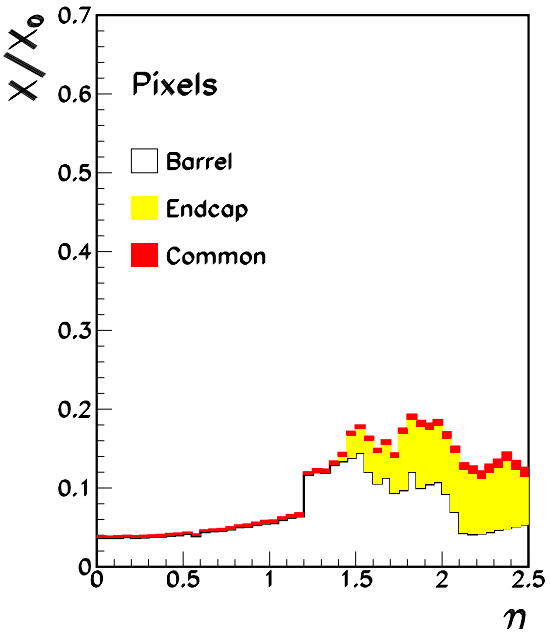

Figure 31: Fractional radiation length contributed by the Pixel system as a function of $|\eta|$.

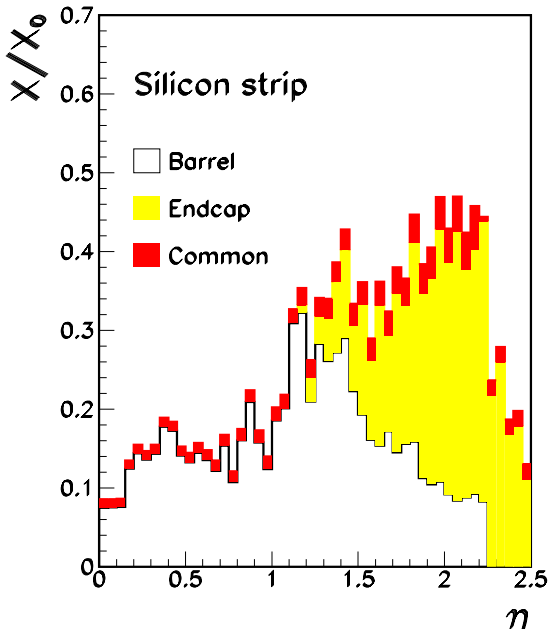

Figure 32: Fractional radiation length contributed by the Inner Silicon system as a function of $|\eta|$.

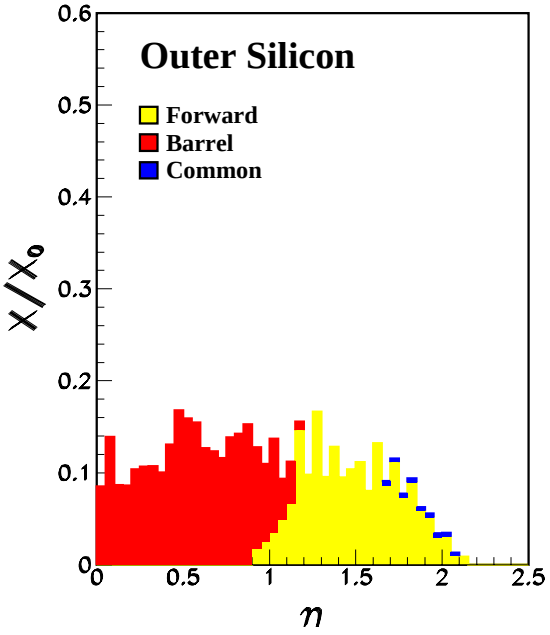

Figure 33: Fractional radiation length contributed by the Outer Silicon detector as a function of $|\eta|$.

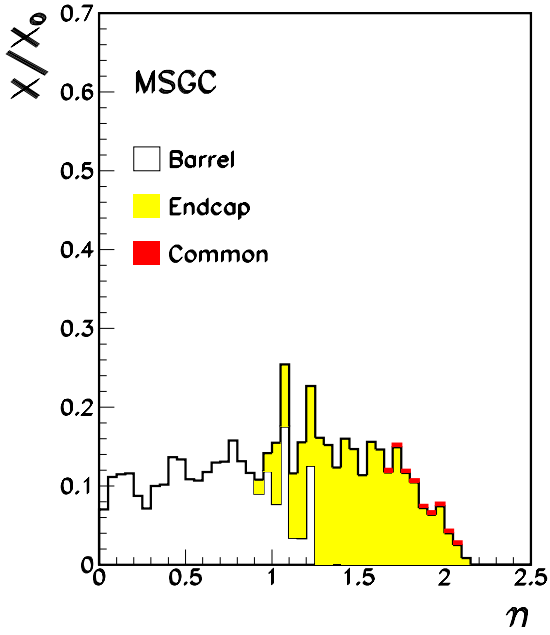

Figure 34: Fractional radiation lengths contributed by the MSGC tracker as a function of $|\eta|$ (pitch $240\mu m$ and $480\mu m$).

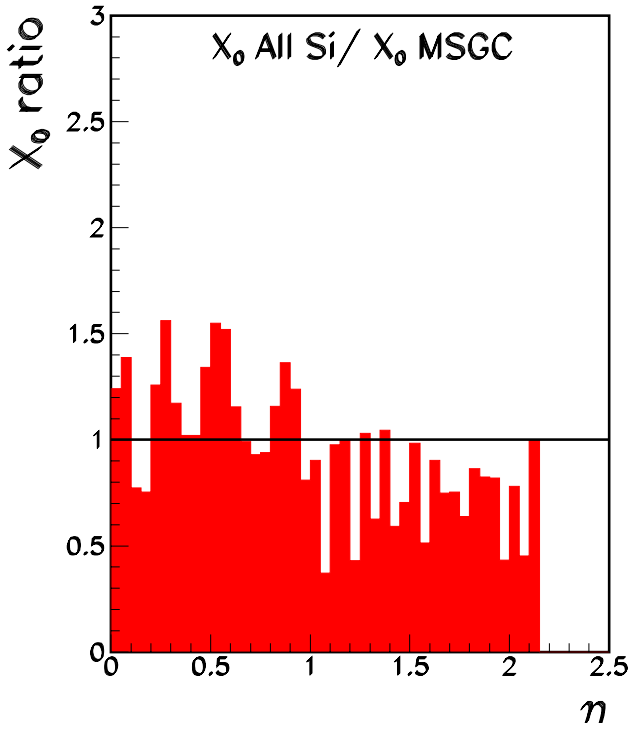

Figure 35: Ratio of the fractional radiation lengths contributed by the outer detectors of the AST and MST layouts as a function of $|\eta|$

6.5 Single hit characteristics

The study of single hit quality is relevant to characterise the intrinsic differences between the MSGC and silicon detectors. We discuss in this section the Monte Carlo model used to evaluate the detector occupancy and we highlight the hit characteristics for the two types of technology.

6.5.1 Hits in silicon micro-strip sensors

The simulation of the silicon sensors has been described in [1]. In the present study the S/N ratio has been set to 10 and "dead" strips have been modelled for all sensors (1%). Single muon tracks have been used for this study and no readout electronics simulation has been implemented. The response of the detectors is illustrated in Figs. 36, 37 and 38 which show the cluster size, hit resolution and the hit reconstruction efficiency as a function of the incidence angle of a track. This study has been done in absence of a magnetic field. This implies that the CMS working point for the outer barrel sensors corresponds to 5 degrees. This value is obtained by considering the actual detector tilt of 12 degrees and the Lorentz angle of the charge carriers amounting to $\simeq 7$ degrees. The data shown by star symbols correspond to the choice of pitch and thickness of the outer detector sensors. The average RMS of hits reconstructed in these sensors is shown to be $\simeq 30\ \mu m$, corresponding to a cluster size of $\simeq 1.3$ strips. The resolution varies moderately as a function of the track angle and even at the largest angle of interest it appears to be well below $100\mu m$. The monotonic behaviour of the cluster size shows the absence of cluster splitting at all angles, as expected (Fig. 36). The hit efficiency is consistently very high and larger than 99 % for angles $< 30^o$ (Fig. 38).

6.5.2 Hits in MSGCs

The CMS MSGC performance estimates reported in [1] were obtained without a complete simulation of the signal deconvolution logic [9]. Its effect was approximated by an appropriate choice of the signal to noise ratio, but the contribution from off- time bunch crossing events could not be properly taken into account. The analysis presented here was obtained with ORCA, which enables pile-up of off-time bunch crossing interactions. In addition, the simulation of the MSGC response in ORCA includes a detailed implementation of the signal deconvolution.

The simulation of MSGC detector response is done in several steps as described in [12] and in [1]. Issues relevant to the subject of this analysis are discussed in [10].

A sample of hits produced by single minimum ionising particles (mip's) has been simulated with a stand-alone program. A 4 T magnetic field was applied. The thresholds for the clustering

procedure have been optimised for the hit efficiency. When more than one cluster is reconstructed, the one closest to the particle impact point is considered. The S/N at optimal angle is 12 in the deconvolution mode.

Fig. 39 shows the hit reconstruction efficiency as a function of the particle incidence angle.

Figs. 40 and 41 show the cluster multiplicity and the size as a function of the particle incidence angle. Figure 42 shows the hit resolution. The cluster multiplicity is minimum and constant within 15 degrees around the drift direction. The multiplicity offset of 0.5 hits per event is due to the noise and is independent of the number of tracks crossing the detector. Clusters split as their charge tends to be shared on more than three strips when the incidence angle is larger than 30 degrees. The hit resolution increases with the angle between the track and the carrier drift direction. It is at best 30 μm. Low p_T tracks tend to reach the outermost barrel layers at large angles, e.g. 40 degrees and 20 degrees when p_T is 1 and 2 GeV respectively. In these cases, the hit efficiency is still good, but the hit quality is poor.

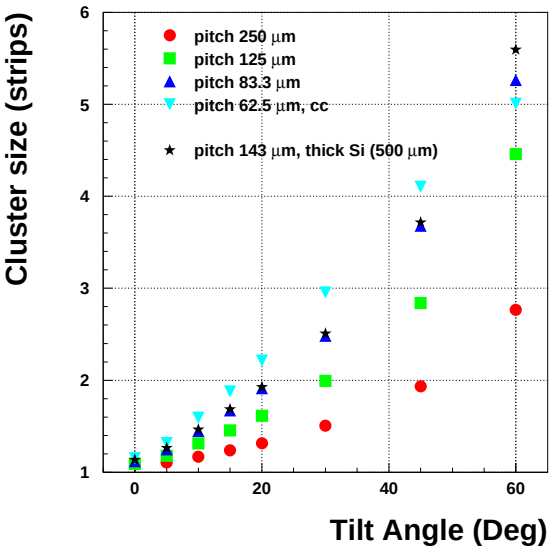

Figure 36: Cluster size in silicon sensors as a function of the track incidence angle. The response has been estimated for several pitch values.

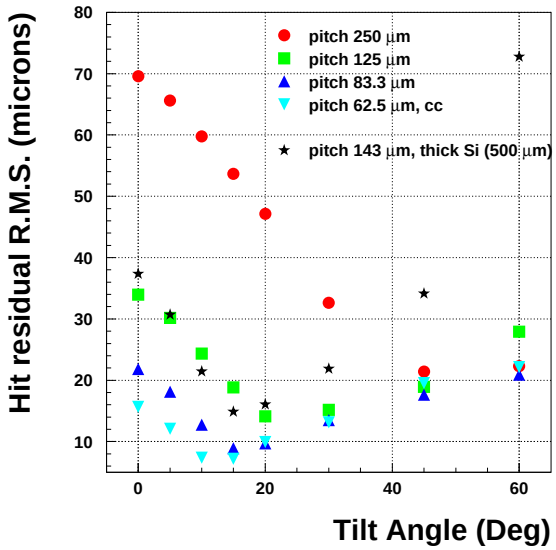

Figure 37: Hit resolution in silicon sensors as a function of the track incidence angle. The response has been estimated for several pitch values.

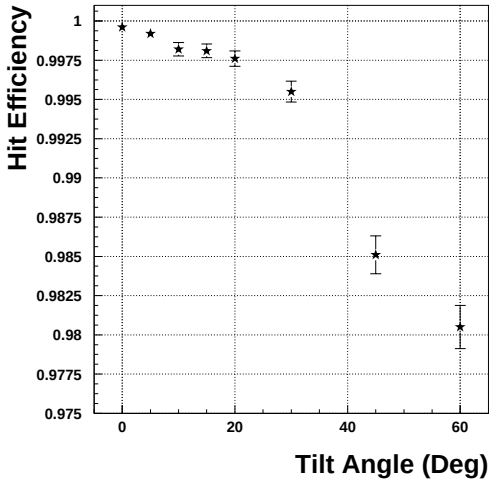

Figure 38: Hit reconstruction efficiency in silicon sensors as a function of the track incidence angle. The response has been estimated for several pitch values.

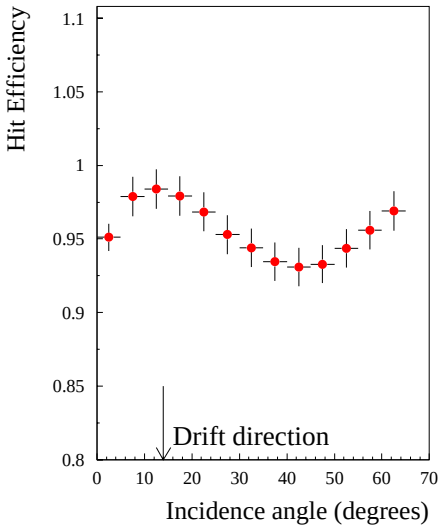

Figure 39: MSGC hit reconstruction efficiency as a function of the particle incidence angle for mip's (0.6 GeV π^-), B=4T, with clustering thresholds 1.4-0.-4. On-time noise has been simulated.

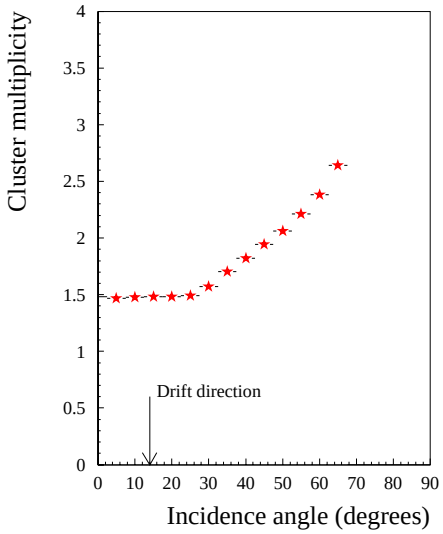

Figure 40: Cluster multiplicity in an MSGC with 0.02 cm pitch, as a function of the particle incidence angle, for mip's (0.6 GeV π^-). Deconvolution mode, with clustering thresholds 1.4-0.-4, B=4T.

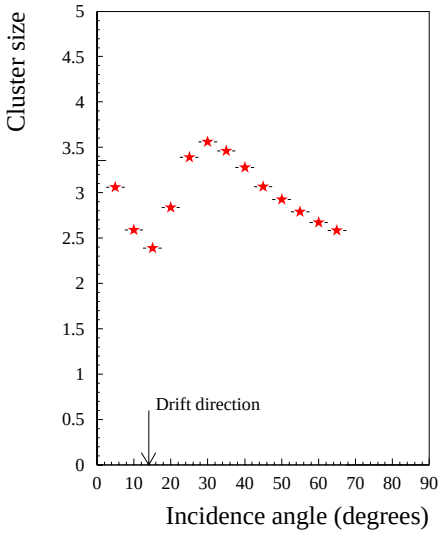

Figure 41: Cluster size in an MSGC with 0.02 cm pitch, as a function of the particle incidence angle, for mip's (0.6 GeV π^-). Deconvolution mode, with clustering thresholds 1.4-0.-4, B=4T.

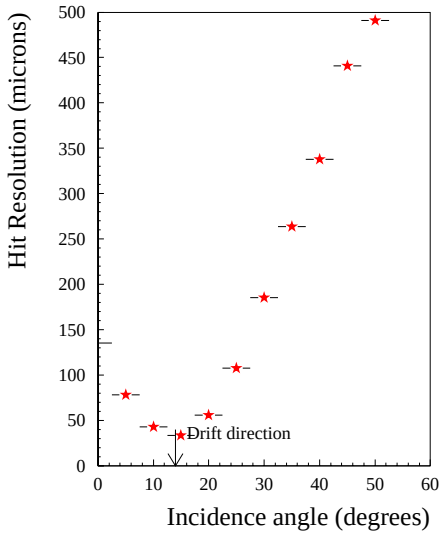

Figure 42: MSGC position resolution as a function of the particle incidence angle, for mip's (0.6 GeV π^-). Deconvolution mode, with clustering thresholds 1.4-0.-4, B=4T.

6.6 Occupancy

The occupancy in high luminosity minimum bias events [2] has been evaluated in the AST and MST layouts. The occupancy is estimated after digitisation and cluster reconstruction, and it is defined as

$$\text{Occupancy} = \frac{\text{Total number of strips in reconstructed clusters}}{\text{Total number of strips}}$$

The denominators could be either the total number of channels or the subset including only strips in hit detectors. Hereafter the occupancy obtained with such definitions will be called respectively *global* and *local* occupancy. The global occupancy is relevant to data acquisition, since it is related to the total data volume, while the local occupancy is related to pattern recognition as it characterises local combinatorics. With respect to the occupancy studies previously done, the effects of signal deconvolution in the APV chip has been taken into account in the simulation of both silicon and MSGC detectors.

The estimated occupancy in AST is shown in Fig. 43 and can be compared to previous results reported in [1]-Figs.7.63 to 7.66. In this study, the simulated pile-up includes 3 early and 2 late bunch crossings.

In contrast to silicon detectors, the impact of "early" and "late" hits on the MSGC occupancy is large. For this reason a more detailed discussion of the event simulation is reported here. The occupancy analysis reported in [1] was obtained using S/N=18. In order to simulate the contribution of early signals, 48 minimum bias events were superposed with Poisson statistical fluctuations and propagated in the MSGC tracker for 500 ns. The values used in this analysis are discussed in section 6.5.2. The number of tracks processed per trigger bunch crossing is given by 24 minimum bias events per bunch crossing (with Poisson fluctuations), taking into account 10 bunch crossings before the trigger and 2 after. In figure 44 the reconstruction efficiency is given as a function of the time of arrival of the particle to the chamber. Noise generated "on-time", i.e. at the trigger time, has also been simulated. A simulated hit was considered as being reconstructed if it had contributed the equivalent of at least 1/2 ADC count to the charge of at least one cluster. The non-negligible probability to find a cluster generated by a track at negative impact times is dominated by the presence of positive crosstalk contributions [10]. The hit S/N ratio as a function of the particle time of arrival to the chamber is shown in Fig. 45.

In view of these results indicating a sensitivity of the deconvolution process to more than three bunch crossings, the factor 2 used in the TDR (the superposition of 48 minimum bias events) is under-estimated.

[2] The definition of minimum bias events can be found [1], section 7.11.2.1, p.462

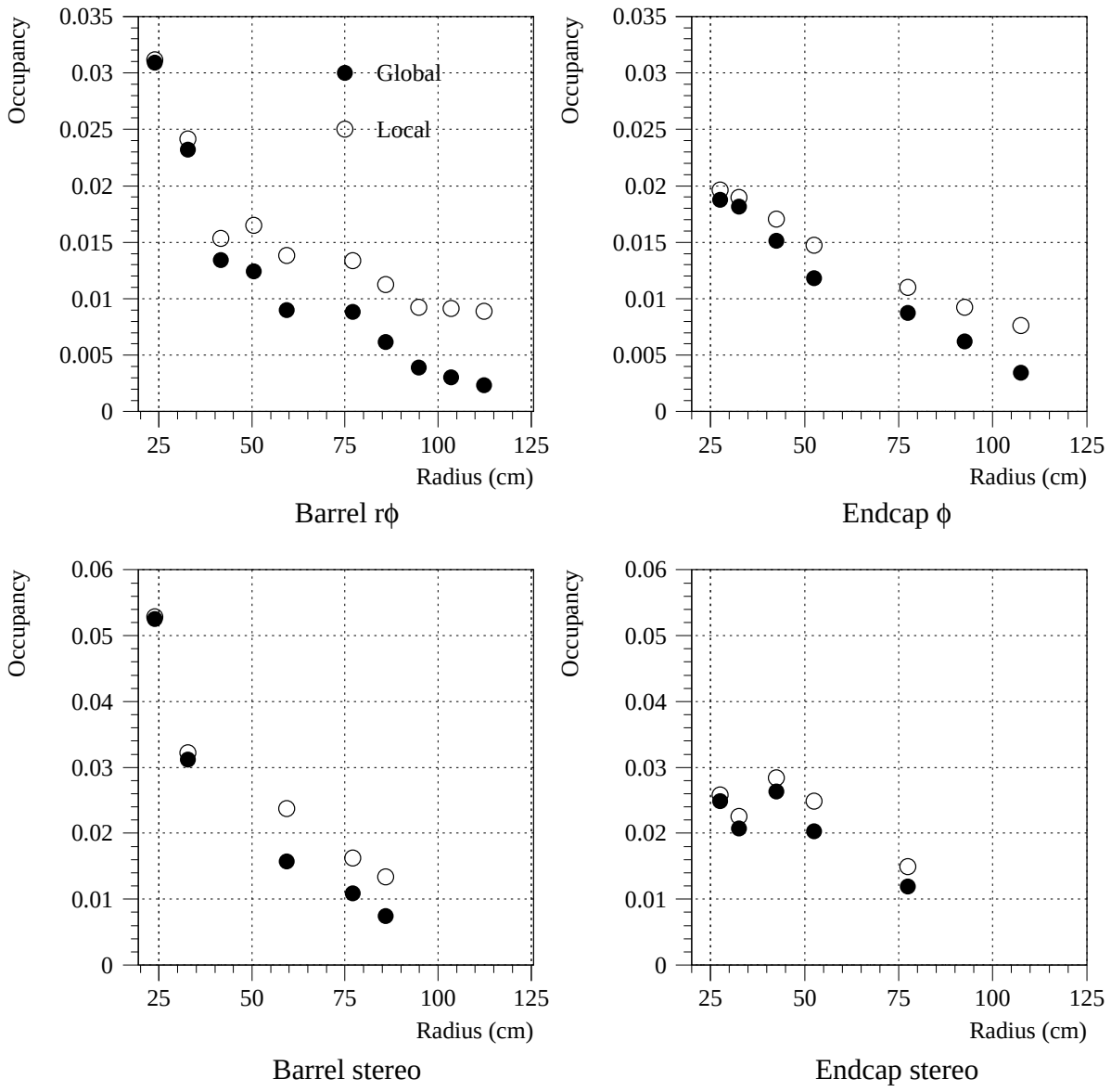

Figure 43: Occupancy in the all-silicon tracker as a function of detector radius. Deconvolution is taken into account. Open and closed symbols represent the global and local occupancy respectively.

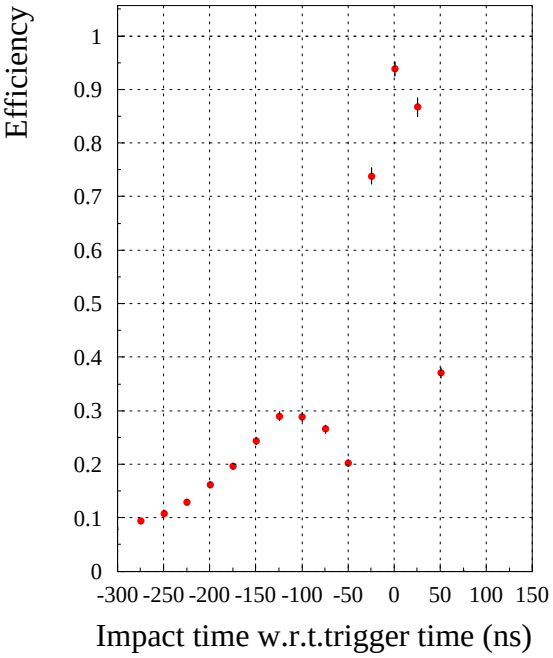

Figure 44: Hit reconstruction efficiency as a function of impact time for mip's (0.6 GeV π^-) crossing an MSGC chamber at normal incidence, B=4T, with clustering thresholds 1.4-0.-4.On-time noise has been simulated

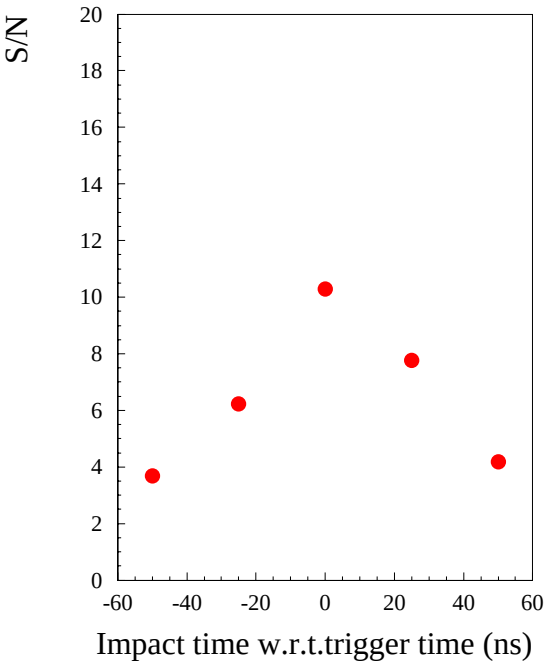

Figure 45: Signal to Noise ratio as a function of impact time for mip's (0.6 GeV π^-) crossing an MSGC chamber at normal incidence, B=4T, with clustering thresholds 1.4-0.-4. No noise has been simulated.

Results are shown for both the TDR approximation (dots) and the ORCA detailed simulation (stars) in Fig. 46. In both cases, "on-time" noise is simulated in all detectors.

As expected, the contribution of hits from out-of-time minimum bias events appears to increase the values of the occupancy estimated in [1], both for silicon micro-strip and MSGC detectors. The local occupancy, in particular, increases between 10% and 30% in the silicon inner tracker and between 30% and 100% in the MSGC's, the latter being more affected by out-of-time hits.

A comparison of the occupancy in the AST and MST outer detectors shows that the local occupancy is a factor between 2 and 5 larger in the MSGC layout than in the all-silicon layout. The global data volume is also reduced in the all-silicon layout, since the number of channels is about the same as with MSGC's, but the global occupancy is lower by a factor two or more.

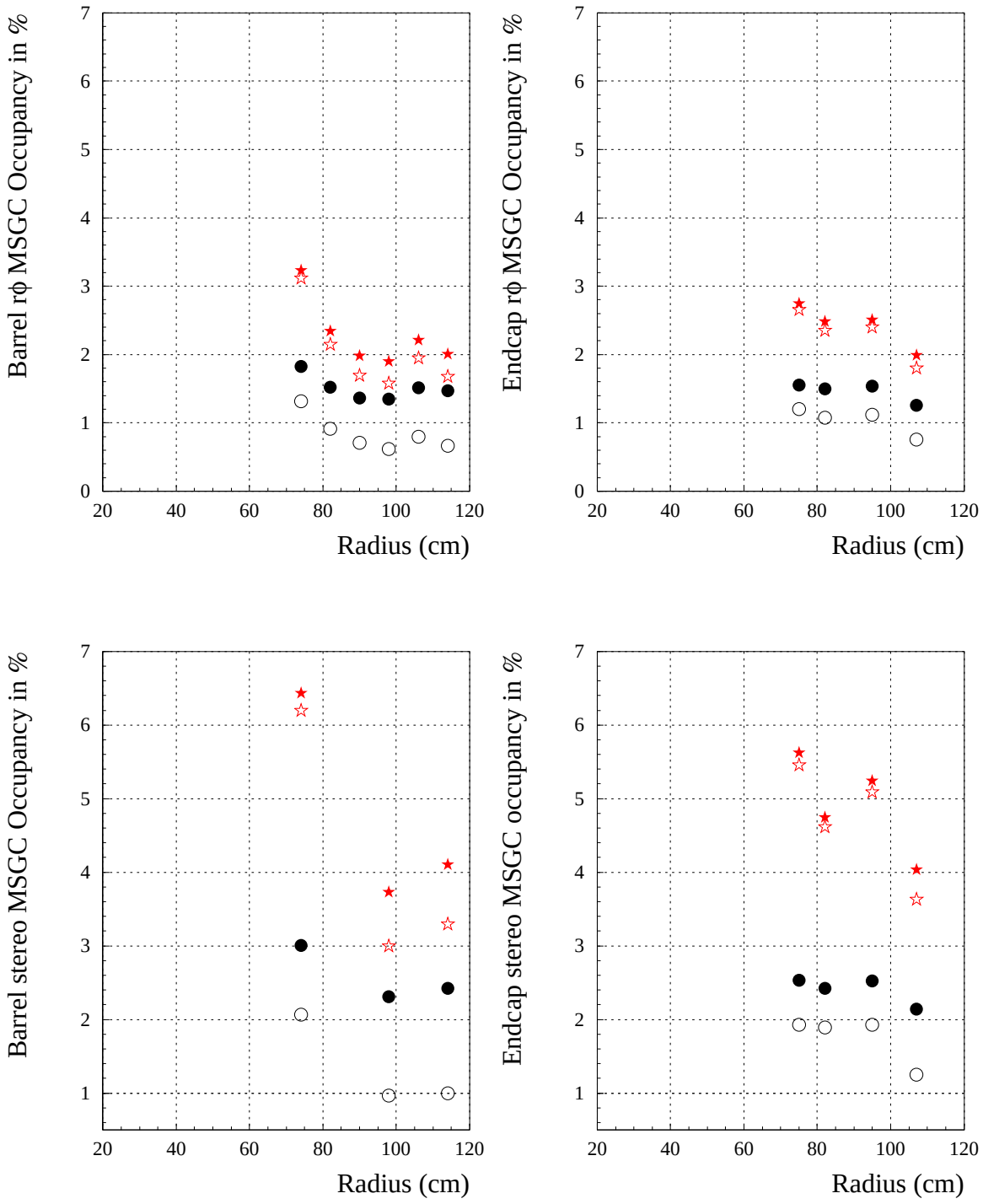

Figure 46: MSGC occupancy in rϕ barrel (left) and end-cap (right) detectors as a function of detector radius. Average values are calculated considering all detectors (open symbols) or exclusively detectors crossed by at least one track (close symbols). (Circles = TDR approximation; stars = ORCA detailed simulation, with pile-up of 10 bunch-crossings before the trigger event and 2 after.)

6.7 Single Track Performance

The evaluation of the single track reconstruction performance is a basic benchmark to probe the performance of a layout. Indeed, the study of the response to a very simple and clean topology allows to disentangle the effects of layout characteristics from the biases of the track finding algorithm. We report in the following a study of the precision of the track parameter estimates and of the single track reconstruction efficiency.

6.7.1 Track measurement precision

The precision of the track reconstruction performance has been evaluated studying single muon tracks of several p_T values. The studies are reported in Figs. 47 to 51. Each figure shows the AST performance in the left plot and the ratio to the MST performance in the right plot. Each point in the histograms has been obtained accumulating a statistics of 500 tracks (errors not shown). The performance is quite comparable for the parameters that measure the track in the $r-\phi$ plane. The parameters that measure the track in the $r-z$ plane are better estimated for tracks crossing the AST layout. The size of the improvement depends on the track p_T and is consistently observable in the plots, keeping in mind that at $p_T < 30$ GeV multiple scattering effects become important. This improvement is due to the better hit resolution in the z-coordinate measured by the silicon sensors.

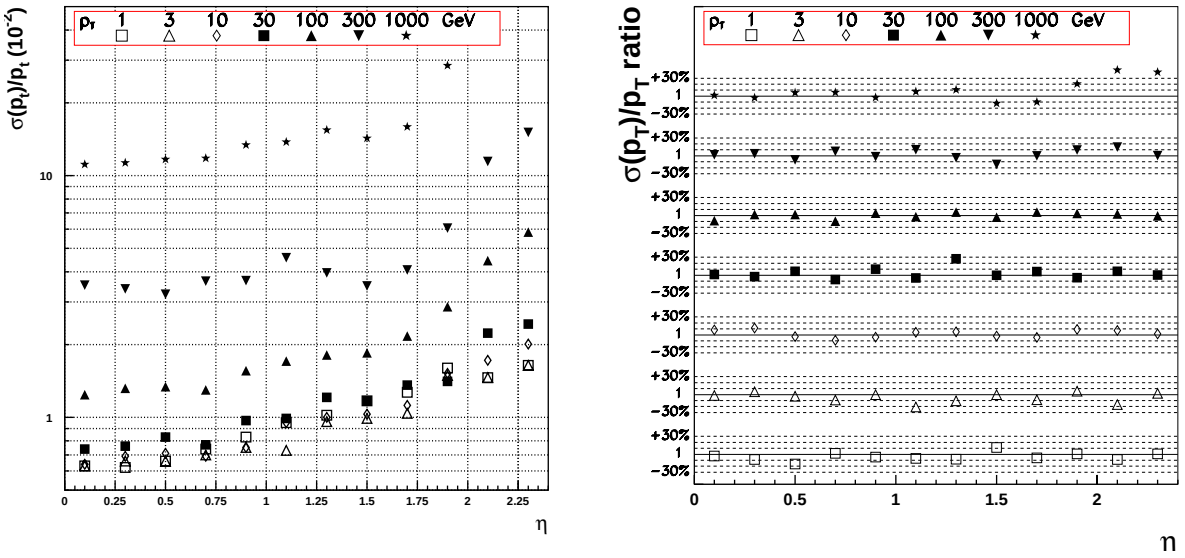

Figure 47: Transverse momentum resolution as a function of detector pseudorapidity. Isolated muons of several p_T values have been reconstructed using the AST layout. The ratio of the performance AST/MST is shown in the right hand side plot.

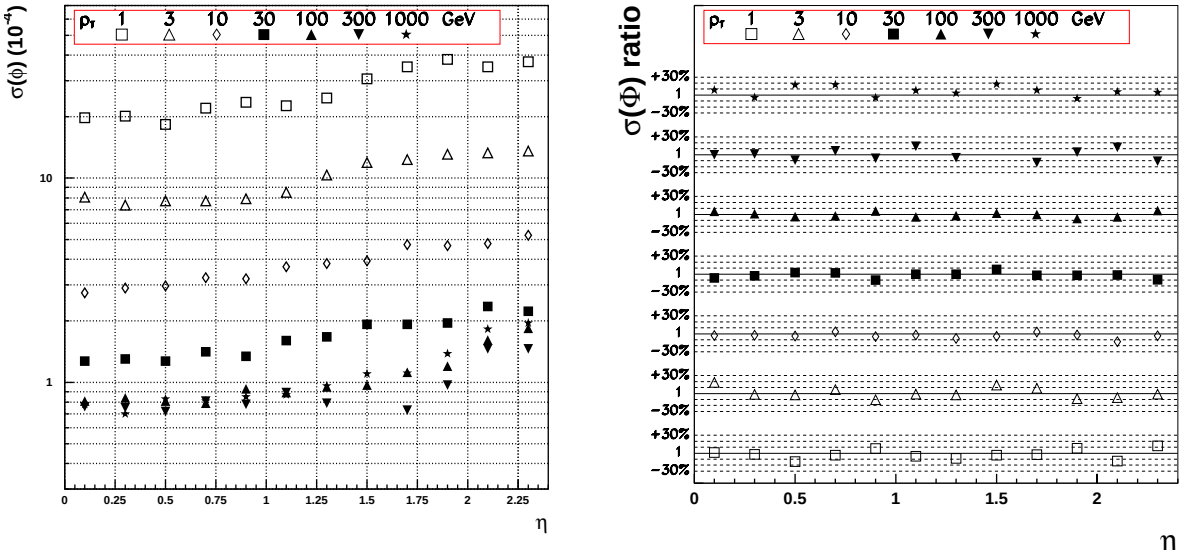

Figure 48: Azimuthal angle resolution as a function of detector pseudorapidity. Isolated muons of several p_T values have been reconstructed using the AST layout (left). The ratio of the performance AST/MST is shown in the right hand side plot.

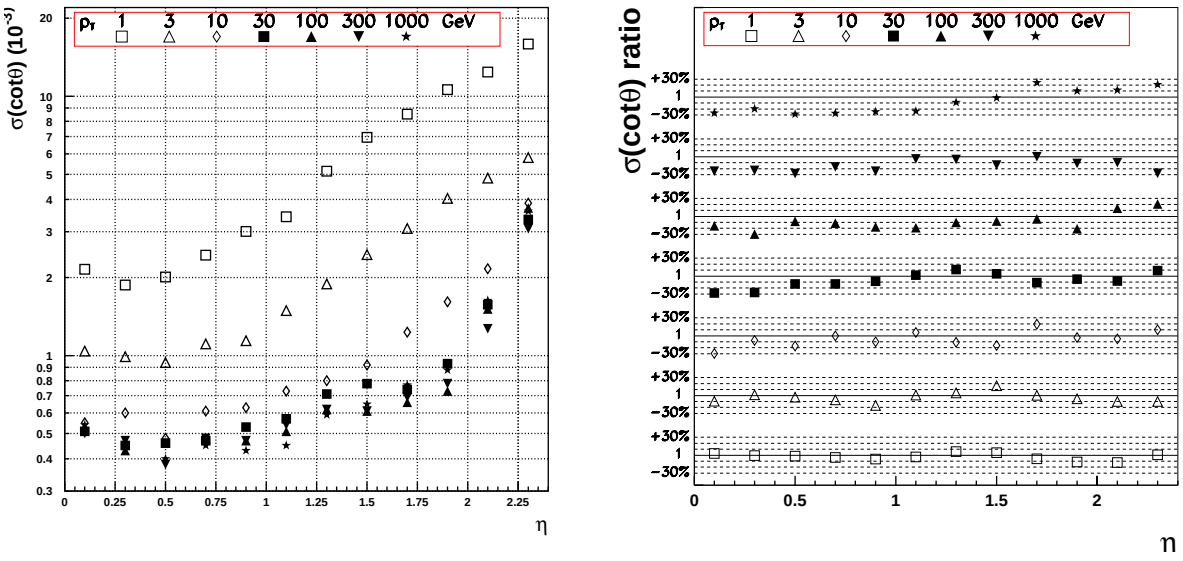

Figure 49: *cotθ* resolution as a function of detector pseudorapidity. Isolated muons of several p_T values have been reconstructed using the AST layout (left). The ratio of the performance AST/MST is shown in the right hand side plot.

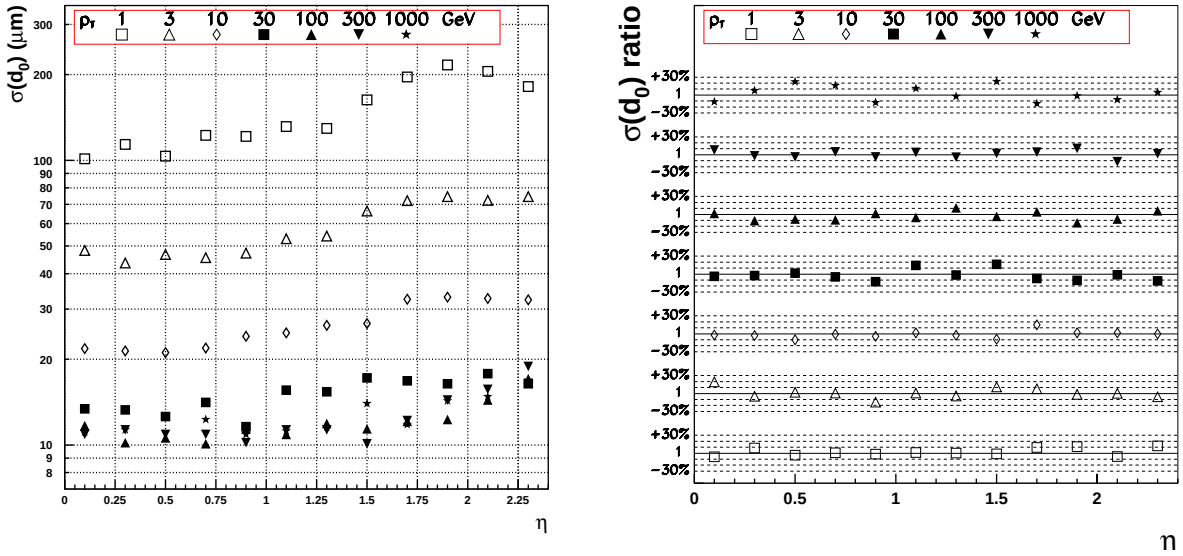

Figure 50: Transverse impact parameter resolution as a function of detector pseudorapidity. Isolated muons of several p_T values have been reconstructed using the AST layout (left). The ratio of the performance AST/MST is shown in the right hand side plot.

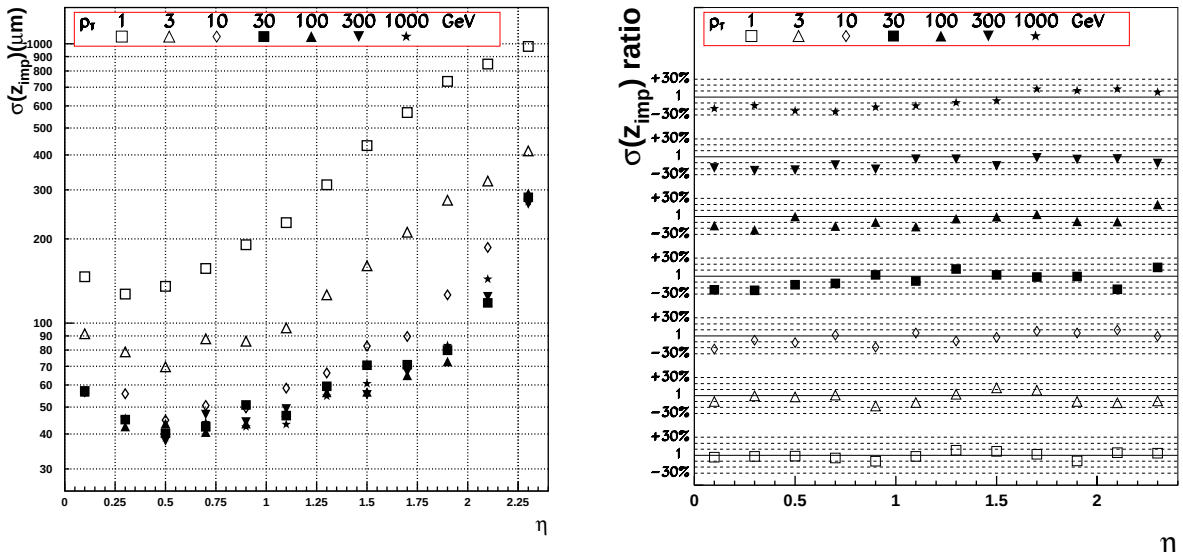

Figure 51: z_{imp} resolution as a function of detector pseudorapidity. Isolated muons of several p_T values have been reconstructed using the AST layout (left). The ratio of the performance AST/MST is shown in the right hand side plot.

6.7.2 Reconstruction efficiency

The single track reconstruction efficiency has been estimated using samples of muons with transverse momentum ranging from 1 GeV to 1 TeV. Muons have been propagated through the AST and MST layouts and tracks have been reconstructed by using the GTF track finding algorithms [1] and requiring at least eight hits be associated with each track. The estimated performance for the AST layout is shown in Fig 52. As discussed in [1], two definitions of efficiency are used. To probe the number of correct hits used in the fits, we define the "efficiency by hits". In this case a track is found when more than half of the associated hits are actually generated by one simulated helix. To check the quality of the fit we define an "efficiency by pulls". In this case a track is found when all track parameters satisfy simultaneously

$$\frac{P_i(fit) - P_i(true)}{\sigma(P_i(fit))} \leq 10$$

where P_i are the track parameters, *true* and *fit* refer to the generated and fitted track and σ is the fit error. This criterion assesses a likelihood of the reconstructed track to the generated helix. The likelihood cut can be tuned to specific topologies and requirements.

A comparison of the AST and MST performance can be found in Figs. 53 and 54 which show the ratio of the AST to MST efficiency, associating tracks by hits and by pulls respectively. The efficiency by hits evaluated for the two layouts is comparable over all the η range.

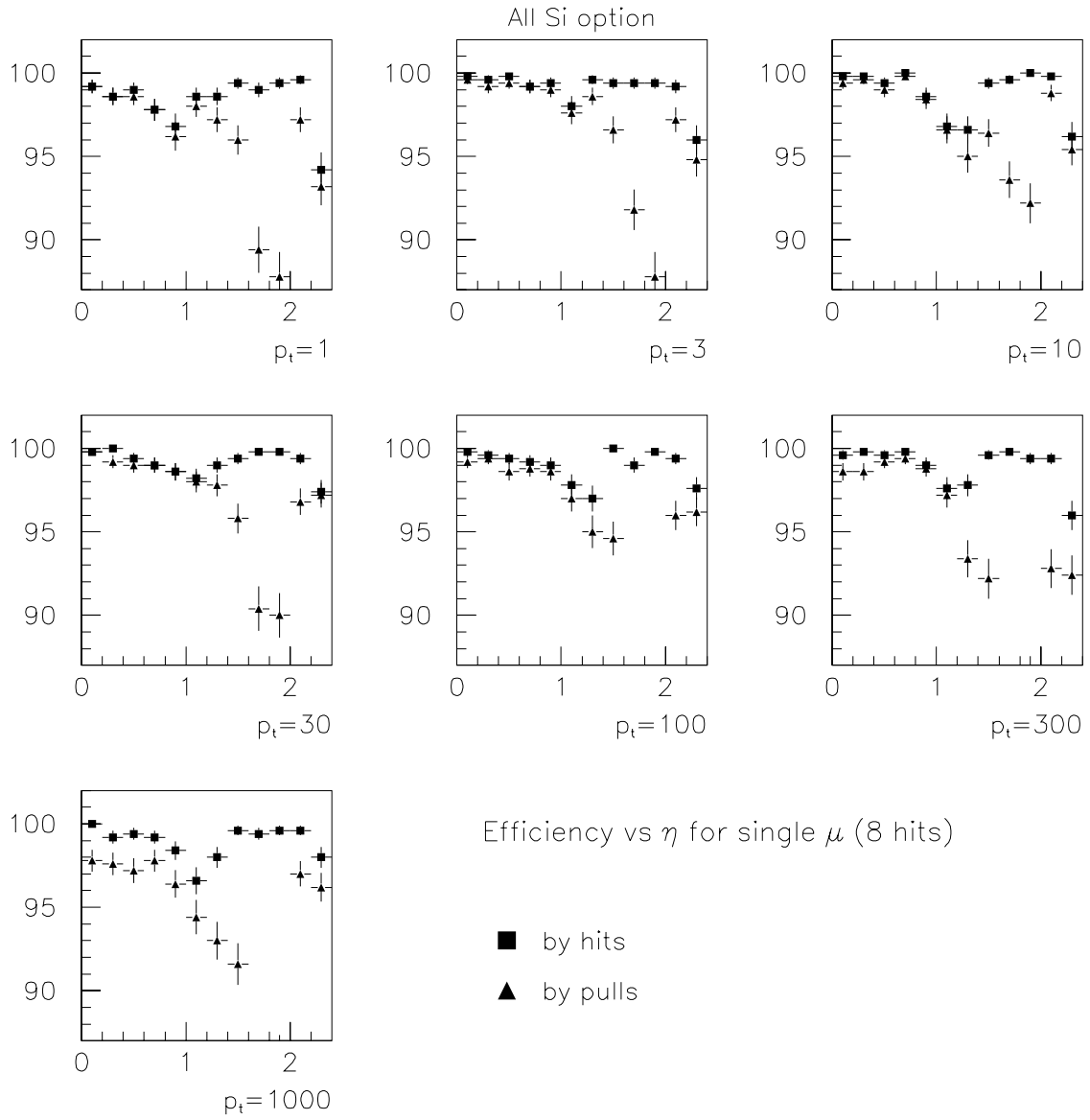

Figure 52: Efficiency to reconstruct single muon tracks crossing the AST layout. The study is performed as a function of η and track p_T. The efficiency is defined in the text.

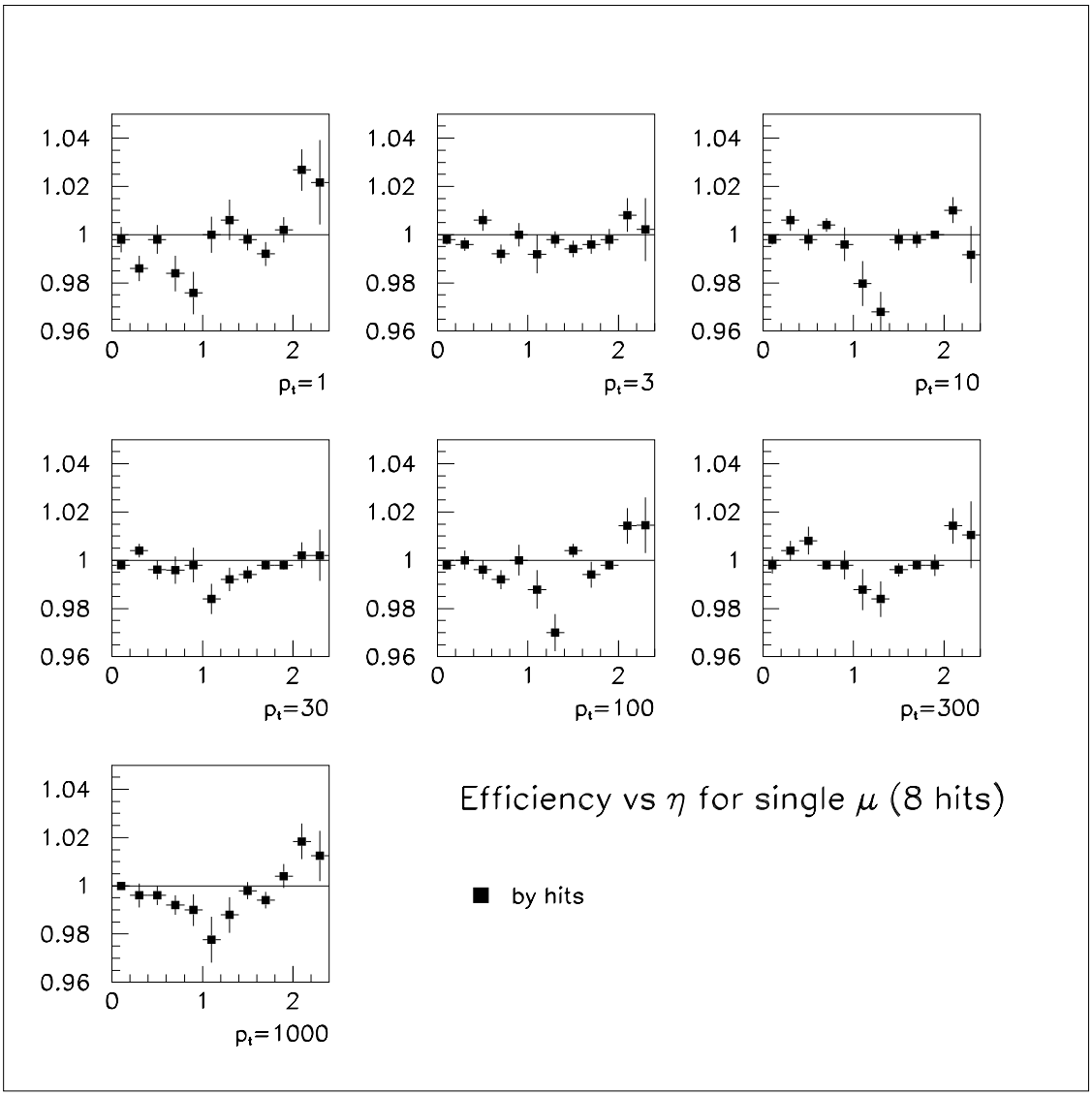

Figure 53: Ratio AST/MST of the efficiency to reconstruct single muon tracks. Tracks are associated by hits.

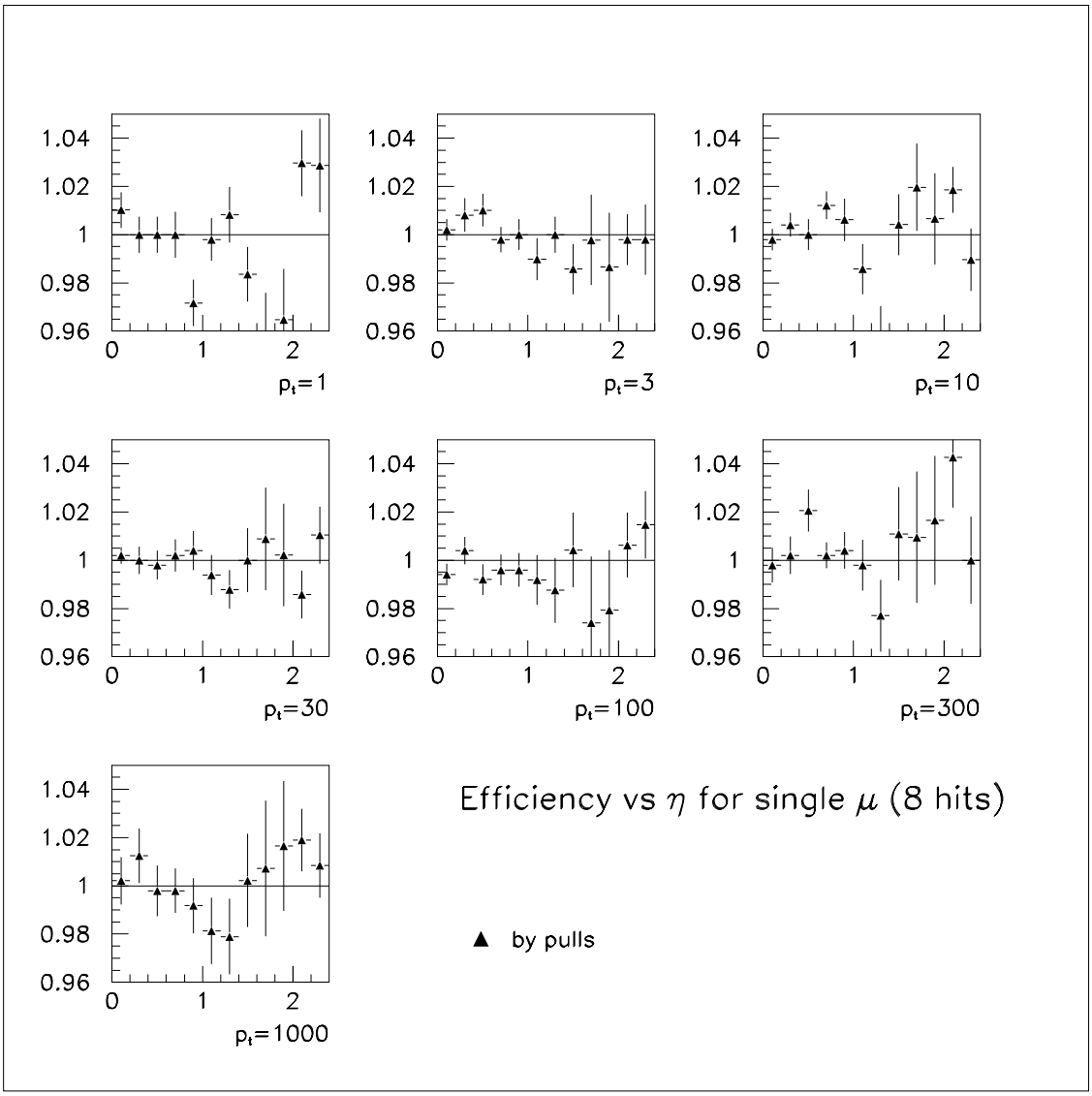

Figure 54: Ratio AST/MST of the efficiency to reconstruct single muon tracks. Tracks are associated by pulls.

6.8 Track Finding Efficiency in Jets

To study the performance of the tracker in a dense hit environment, a sample of $E_T = 200\ GeV$ jets has been used. In this case, no additional pile-up has been added to the hard interaction in addition to the underlying event. The detector response has been simulated without taking into account deconvolution effects. Tracks have been reconstructed with CM-FKF [1], requiring tracks to register at least eight hits in the AST and MST layouts. The efficiency definition has been discussed in the previous paragraph and the fake rate is defined consistently to what reported in [1]-Section 9.5.2. The track finding efficiencies and fake rates for tracks in 200 GeV E_T jets are shown in Tables 12, 13, 14 and 15. The study has been performed also requiring tracks with at least six hits to illustrate the dependence of this analysis on the number of sensitive layers in each layout. Requiring "longer" tracks highlights the role of the outer detector in track reconstruction, which mainly consists of solving ambiguities as can be shown by the fake rates reported in the tables. The performance of the two layouts in terms of efficiency and fake rate is fully comparable.

	$\|\eta\| < 0.7$	$1.2 < \|\eta\| < 1.6$
TDR Tracker	88.2 ± 0.7	85.9 ± 0.8
	null	0.05 ± 0.05
All-silicon Tracker	88.3 ± 0.9	86.8 ± 0.8
	0.06 ± 0.06	0.10 ± 0.07

Table 12: Track reconstruction performance in 200 GeV E_T jets as a function of detector pseudo-rapidity. Tracks are associated to their parent helix by requiring 50% common hits. In each table slot the upper number represents the tracking efficiency and the second the ghost rate, expressed in percent. Reconstructed tracks are required to register at least eight hits in the detector.

	$\|\eta\| < 0.7$	$1.2 < \|\eta\| < 1.6$
TDR Tracker	93.0 ± 0.6	90.6 ± 0.7
	0.4 ± 0.1	0.24 ± 0.11
All-silicon Tracker	93.7 ± 0.6	91.6 ± 0.6
	0.26 ± 0.09	0.10 ± 0.07

Table 13: Track reconstruction performance in 200 GeV E_T jets as a function of detector pseudo-rapidity. Tracks are associated to their parent helix by requiring 50% common hits. Reconstructed tracks are required to register at least six hits in the detector.

	$\|\eta\| < 0.7$	$1.2 < \|\eta\| < 1.6$
TDR Tracker	84.2 ± 0.9	81.7 ± 0.9
	7.3 ± 0.6	6.8 ± 0.6
All-silicon Tracker	85.2 ± 0.9	83.1 ± 0.9
	5.2 ± 0.5	7.3 ± 0.6

Table 14: Track reconstruction performance in 200 GeV E_T jets as a function of detector pseudorapidity. Tracks are associated to their parent helix by requiring all track parameter pulls to satisfy simultaneously the condition $\sigma < 10$. Reconstructed tracks are required to register at least eight hits in the detector.

	$\|\eta\| < 0.7$	$1.2 < \|\eta\| < 1.6$
TDR Tracker	88.6 ± 0.8	85.6 ± 0.8
	8.4 ± 0.6	9.5 ± 0.6
All-silicon Tracker	90.6 ± 0.7	87.4 ± 0.8
	6.1 ± 0.6	8.9 ± 0.6

Table 15: Track reconstruction performance in 200 GeV E_T jets as a function of detector pseudorapidity. Tracks are associated to their parent helix by requiring all track parameter pulls to satisfy simultaneously the condition $\sigma < 10$. Reconstructed tracks are required to register at least six hits in the detector.

6.9 Reconstruction of $B \to J/\psi K^0_S$

A sample of $J/\psi K^0_S$ has been generated and reconstructed according to what described in the Tracker Technical Design Report, Sec. 9.6.3. The decay topology is

$$J/\psi K^0_S \to \mu^+\mu^-\pi^+\pi^-$$

where a semi-leptonic decays is forced on the accompanying b partner to ensure trigger capability. The B meson finding efficiency is defined by the number of correctly reconstructed B_d with mass within a window of 50 MeV around the PDG value. Similarly, the J/ψ and K^0_S mass values are required to be within 70 MeV and 25 MeV of their nominal value, respectively.

Table 16: Efficiency to reconstruct $B_d \to J/\psi K^0_S$ using the all-silicon and V4 tracker layouts.

	Efficiency (%)
TDR Tracker	32.6 ± 1.2
All-silicon Tracker	36.3 ± 1.2

The difference in efficiency is mainly due to the better performance of the all-silicon barrel tracker in reconstructing K^0_S. Better hit resolution and efficiency for low p_T tracks appears to compensate

for the smaller number of detecting layers. In the end-caps, the performance of the two layouts is comparable. This study is preliminary and further work will be dedicated to this issue.

6.10 Reconstruction of converted photons

A study of the reconstruction efficiency is performed using a sample of $3 \cdot 10^4$ photons of $p_T = 30$ GeV generated at $|\eta| < 0.7$. The fraction of converted photons in the Tracker volume is found to be 21.5% and 22.6% in the AST and MST layouts respectively. Tracks are reconstructed using the CM algorithm and requiring that at least five hits be associated with each track in the detector. Pairs of reconstructed tracks of opposite curvature sign are then constrained to a common secondary vertex. The efficiencies are reported in Table 17. The first row gives the efficiency to reconstruct converted photons in both trackers. The second row shows the efficiency to reconstruct converted photons for which the reconstructed z coordinate of the impact point (Z_{prim}) is within 5 cm of the true value. The MST layout is 12% (relative) more efficient than the AST layout, due to the larger number of sensitive planes available in MST. Requiring a Z_{prim} resolution of 0.5 cm, the two efficiencies are equal. It should be noticed that the AST layout has better precision in measuring the reconstructed photons, due to the better resolution of the hit stereo coordinate. This is illustrated in Fig. 55, showing the reconstructed Z_{prim} for photons converting in the two layouts.

Table 17: Efficiency of track selection criteria, intrinsic track finder efficiency and global efficiency to reconstruct photons undergoing conversion in the AST and MST detectors.

Tracker layout	AST	MST
Reconstruction efficiency (%)	54.0	60.8
Reconstruction efficiency (%) within 0.5 cm	38.0	37.0

6.11 Summary

Some aspects of the performance of the AST and MST detector layouts have been compared. It was ascertained that the performance of the two detectors is comparable in what concerns the quality of $r - \phi$ hits generated by tracks with $p_T > 2$ GeV. The single track reconstruction performance is substantially equivalent. Also the efficiency to reconstruct tracks in $E_T = 200$ GeV jets appears to be unaffected by the change of layout. The b-tagging efficiency and fake rate, dominated by the Pixel detector layout, are expected to be the same for the two layouts and are discussed in [1].

The AST layout is superior in the stereo hit quality, hence improving the precision of the track parameters measured in the r-z plane. The better quality of the hits registered by very low p_T

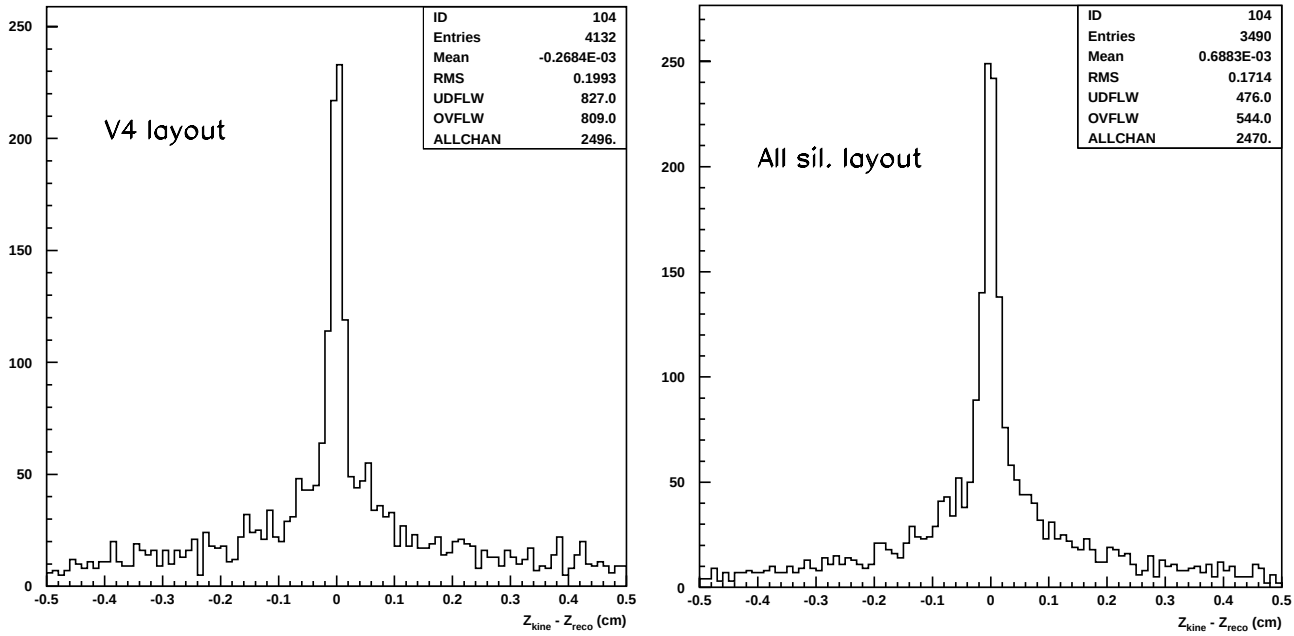

Figure 55: Resolution of the recontructed z impact point for photons that convert to e^+e^- pairs in the MST (left) and AST (right) detectors.

tracks in the AST layout appears to improve the efficiency to reconstruct K_0^S produced in the reaction

$$b\bar{b} \rightarrow J/\psi \; K_S^0 \; \mu + X \rightarrow \mu \; \mu \; \mu \; \pi^+ \; \pi^- + X$$

A study of the occupancy recorded in the two layouts in presence of very high luminosity events shows that the occupancy is lower by at least a factor 2 in the AST detector due to the lower sensitivity to out-of-time events. The impact of this behaviour on the performance of the two detectors has not been evaluated, due to the still imperfect performance of the new reconstruction package implementing the full readout electronics simulation. It is nevertheless to be expected that the performance of the all-silicon tracker in presence of high luminosity events will be comparable to the one reported in [1]. Indeed, the study of the performance in a high hit density environment , i.e. within high E_T jets, reported in this document shows that the lower number of sensitive layers does not affect the ability to reconstruct good and ghost tracks for jet transverse energies as large as 200 GeV. The addition of the high-luminosity pile-up does not appear to affect the performance of MST, as shown in [1]. Since the occupancy due to pile-up is larger in MST than in AST, we do not expect a performance deterioration in AST.

The reconstruction of isolated electrons is expected to be comparable to the one reported in [1], given that the material budget of the AST and MST detector has been shown to be comparable.

Moreover, the present electron track reconstruction algorithm relies mainly on the inner tracker. As discussed in [1], the highest probability to undergo bremstrahlung occurs in the region between the inner and outer tracker volumes, where a large amount of material is contributed by the inner silicon services [3]. In view of electron identification, typically requiring a match between the transverse energy measured in the calorimeter and the p_T of the reconstructed and associated track, the electron track segment reconstructed using the inner tracker has higher likelihood to be linked to the cluster measured in the EM calorimeter.

Muon identification, obtained associating a track segment measured in the muon chambers to a track reconstructed in the Tracker is not affected by the different layout of the double sided layers in the two layouts. In fact, the extrapolation of low p_T muons to the tracker is affected by large uncertainties up to at least 100 GeV muon p_T, due to the large material separating the muon and track detectors. The uncertainty is much larger than the z-precision of the hits reconstructed in the outer tracker layer and defined by the detector segmentation. In the case of high p_T muons ($p_T >$ 100 GeV), the extrapolation error will be much smaller and the difficulty to associate correctly muon tracks in the outer and inner detectors will be simplified by naive p_T matching requirements.

[3] This situation may be improved in the case of the alternative layout shown in Fig. 2

7 Organization of the Construction

The planning for the construction of the all-silicon tracker started at the beginning of January. All the institutions of the existing Tracker collaboration, and new groups from USA (Fermilab, Purdue, Rochester and Northwestern), will participate in the construction.

To date we have produced a detailed Product Breakdown Structure (PBS), but we are not yet ready to show a schedule and a list of Milestones. These will be available by the middle of April.

The schedule for construction is driven by the production of the 20,000 modules. Once all the components are available (sensors, frames, hybrids with the electronics already mounted) the sensors and hybrids have to be precisely assembled on the frames and bonded. We assume that the production will take 2.5 years, corresponding to a total throughput of 40 modules per day. From the market survey of the sensors we know that there are at least two producers that can deliver all the sensors that we need within 2.5 years. The production of the front-end electronics can be done in a shorter time.

The throughput of the robot assembly is 6/8 modules per hour and the throughput of a bonding machine like the Devoltec 6400 is 2 modules per hour. We plan to install at least 6 robots and we have more than 12 bonding machines of the required quality, corresponding to a peak production of 200 modules/day. The real production rate will depend on the rate of failures. Our modules are very simple (single sided, many with large pitch). From the experience of large-scale production of simple modules in Fermilab we consider that a factor of 5 between the achievable peak production rate and the necessary production rate is largely sufficient and includes contingency. Our present plan is to start a pre-production before the end of the year 2000 and ramp up to full production rate during the first half of 2001. This schedule will allow us to deliver the Tracker to CMS by September 2004.

The mechanical support structure can be built in a shorter time. As already discussed in the introduction and in Chapter 5 we are evaluating two different possibilities (one volume versus two separate volumes for the inner and the outer parts). We plan to make a final decision on the layout of the tracker by June 2000, in order to be ready for an Engineering Design Review before the end of the year 2000.

We are currently well advanced in the first phase of our discussions, which is to solicit and collect proposed engagements from all the institutes in the Tracker Collaboration. From the proposals now available it is apparent that the collaboration has enough resources to cover all the tasks to build the Tracker and, that a scheme for the construction exists. The next stage will be to assure the detailed match of the resources to the PBS and to establish of an internal MOU. In the following

the current set of proposed commitments is outlined.

The production of the modules will be shared in three consortia: USA, INFN [4] and CE [5] sharing roughly 1/3 of the production of the modules each. They will deliver modules with burn-in already done. US institutions will build the modules in the Fermilab silicon facility where, in addition to the existing equipment, two robots will be installed. INFN will install robots in Bari and Perugia. CE will install the robots in Brussels and Lyon. The bonding will be shared in several laboratories to exploit the available bonding machines (Aachen, Bari, Florence, Karlsruhe, Padova, Pisa, Strasbourg, Torino and Zurich). Many institutions have volunteered to carry out the burn-in. This will be shared in those laboratories that have the resources available. In addition Finland and Vienna, who have already set up the module production line, offer to produce a fraction of the modules (2.5 % each) with semiautomatic mounting. They will provide the quality control of their production.

The components needed for the production will be produced/tested for the whole tracker under the responsibility of a single institution - which also has the responsibility of defining the final design/specification for that component - with the help of other institutions for the testing (Table 18).

item	institutions
frames	Belgium + Strasbourg
pitch adapters	Belgium
hybrids	Strasbourg and Perugia + Aachen, other institutions for bonding
sensor testing	Pisa and Karlsruhe + Louvaine, Perugia, Strasbourg

Table 18: Breakdown of component responsability. Institutions with the main delivery responsibility are shown first.

The responsibility for the construction of the mechanical structure and module integration on the structures is shown in Table 19.

structure	mechanics	integration of the modules on the structures
overall support mechanics	CERN	
outer barrel	CERN/Finland	CERN/Finland + INFN
inner barrel	Pisa + Fermilab	INFN
forward disks	Aachen	CE + CERN

Table 19: Breakdown of integration responsability.

CERN will have the main responsibility of the overall mechanical integration, cooling, cabling, services and external infrastructures.

[4]The INFN consortium includes Bari, Catania, Firenze, Padova, Perugia, Pisa and Torino

[5]The CE consortium includes Austria: Vienna; Belgium: Brussels UVB, Brussels ULB, Antwerpen, Louvain-La-Neuve, Mons; Germany: Aachen I, Aachen III, Karlsruhe; Finland: Helsinki, Oulu; France: Mulhouse, Lyon, Strasbourg; Switzerland: ETH Zurich

Electronics procurement will be carried out mainly by the UK, for the front end chips and Front End Drivers, and CERN, for remaining ASICs, optical links and elements of the control system. There will be continued participation from several other countries in the remaining developments leading up to production and especially in the assembly, evaluation, testing, installation and commissioning. Other countries will share costs, participate in the management of electronics items and in procuring off-detector electronics, such as control system components (Karlsruhe, Vienna), power supplies (Firenze and Torino), and low mass internal cables (Bari).

7.1 Cost estimate for the All-Silicon Tracker

The cost evaluation for the all-silicon tracker is based on the cost analysis previously carried out for the version of the CMS Tracker described in the TDR. The cost book items list was modified to reflect the change from the TDR layout to the proposed all silicon layout. Component costs are essentially unchanged, except for the significantly reduced costs of:

- the front-end chip, due the adoption of the APV25 and other ASICs in the 0.25um technology
- the silicon sensors, driven mainly by the move to high volume 6" wafer production lines

A further important new input is a new cost estimate for cables and services based on commercial budgetary estimates from a number of firms: these are considerably higher than those previously assumed.

Next, the cost of certain elements, for example the outer Tracker support structures, the thermal screen and cooling plant etc., were appropriately revised, extrapolating from the corresponding items costs in the TDR. The effect of these modifications on the overall cost is, however, relatively minor.

A summary of the cost is given in Table 20, broken down in a similar way to that done for the TDR version of the Tracker. As already discussed, the proposed layout has less active area than the TDR layout. This was done in order to stay within a budgetary ceiling of 77.5MCHF, previously agreed upon by the CMS Collaboration for the Tracker project. It can be seen that, indeed, the detailed cost analysis confirms the earlier estimates on which the proposal was based, and that the cost ceiling is met.

item	cost in kSF
pixel barrel	5'769
pixel forward	2'470
pixel total	8'240
inner Si barrel	11'451
inner Si forward	10'261
inner Si total	21'712
outer Si barrel	23'121
outer Si forward	15'091
outer Si total	38'211
mechanics + infrastructure	9'420
total tracker cost	77'583

Table 20: Cost breakdown.

References

[1] **CERN LHCC/98-6, CMS TDR 5**, CMS Collaboration, *"CMS: The Tracker Project: Technical Design Report"*

[2] M. Huhtinen and F.Faccio, *Computational method to estimate Single Event Upset rates in an accelerator environment*, accepted for publication in NIM A. Available at http://cmsdoc.cern.ch/∼huu/seu.ps.

[3] S. Braibant et al., Investigation of design parameters and choice of substrate resistivity and crystal orientation for the CMS silicon microstrip detector, CMS NOTE 2000/011.

[4] E. Barberis et al., Nucl. Instr. and Meth. in Phys. Res. A 342 (1994) 90.

[5] A. Carraro et al., "Design of the thermal screen for the CMS tracker", CMS Internal Note in preparation.

[6] H. Breuker et al., TK Engineering Meeting, 1999 - 080, October 12th 1999.

[7] CMSIM User's Manual and Reference Guide

[8] GEANT3 - Detector Description and Simulation Tool, CERN program Library entry W5013, CERN Geneva, Ed. March 1995.
R. Brun et al., GEANT3, CERN DD//EE/84-1, revised 1987

[9] See for example "The Tracker Project Technical Design Report", Section 5.3.4 and references therein.

[10] **CMS Note 2000/015** V. Lefebure, *"Simulation of MSGC sugnals in CMS"*

[11] **CMS Internal Note, CMS/IN 99/35**, D.Stickland, *"CMS Reconstruction Software: The ORCA project"*

[12] **CMS Internal Note, CMS/IN 2000/016** with reference to [13] and to [14], V.Lefébure, *"MSGC response simulation in ORCA"*

[13] **INFN PI/AE-94/02**, R.Bellazzini and M.A.Spezziga, *"Electric field, avalanche growth and signal development in Micro-Strip Gas Chamber and Micro-Gap Chamber"*

[14] **NATO-ASI Series, B:Physics Vol.365, Ed. Thomas Ferbel, 1997** *Techniques and Concepts of HEP*

A Radiation environment and detector considerations

The experimental conditions in the region of radial distance from the beam line 70 mm $\leq R \leq$ 1150 mm have been already described in the TDR. Here we recall the basic features of the operating environment in the outer tracker.

The radiation environment in the outer Tracker and the methods used to calculate it have been discussed in depth in the TDR. However, since the writing of the TDR technical designs of the polyethylene moderators lining the ECAL have been worked out in more detail. Since the damage in silicon is dominated by charged hadrons up to a radius of about 50 cm these moderators have only a reduced effect on the inner silicon. Because MSGC – contrary to silicon – are not particularly sensitive to neutrons around 1 MeV it was accepted that the effective thickness of the moderators can be slightly less than the design value.

In the TDR we specified a barrel moderator thickness of 30 mm. Later it was agreed that this space could be used to route the optical fibers of the ECAL and the space between the fibers would be filled with polyethylene powder. Given a slight reduction of nominal thickness and a best guess for the filling fraction, the remaining effective polyethylene thickness is about 15 mm. The endcap moderators will be paraffin-filled aluminium honeycombs. Measurements have shown that a filling fraction of almost 90 % can be reached. This gives an effective thickness of (35+35) mm instead of the (40+40) mm assumed in the TDR.

With silicon detectors also in the outer, neutron dominated, region these moderator reductions are not negligible and require new simulations, the results of which are summarized in Tables 21 and 22. The rows labeled 'hadrons E>E_{thres}' show the sum of the first four rows and the neutron flux with the corresponding cut-off E_{thres}.

As could be expected the charged hadron fluences agree with those presented in the TDR but the neutron fluence exhibits a clear increase due to the thinner moderators. It should be noted that a corresponding fluence increase is observed also at the inner silicon, but here it is overwhelmed by the large charged hadron fluence. For instance for the lowest edge of the last inner endcap disk the TDR gives as the total fluence of fast hadrons $(12.1 \pm 0.2) \times 10^{13}$ cm^{-2} which now has increased to $(13.7 \pm 0.8) \times 10^{13}$ cm^{-2}, i.e. by ∼15% only.

Compared to the tables presented in the TDR we now also show neutrons above 20 MeV separately. This is motivated by recent studies which indicate that Single Event Upsets might occur at a non-negligible rate and that in most components this rate scales rather well with the total hadron flux above 20 MeV threshold [2].

The uncertainties of the radiation estimates have been discussed in the TDR. We recall that we

recommended a general safety factor of about 1.5 but pointed out that this should be increased towards the outer tracker where neutron albedo dominates. Our new results verify that the values indeed are quite sensitive to the exact geometry and in particular the moderator configuration. Thus it seems well motivated to recommend a safety factor of 2 for the outer Tracker. Thus the sensors of the outer Tracker should be specified for a '1 MeV neutron equivalent' flux of about 5×10^{13} cm^{-2}. This covers the outer barrel and most of the outer endcap with sufficient safety factor. Although these radiation levels are important, they still are a factor of 5 below the maxima expected in the inner tracker (with safety factor 1.5 applied). This difference has an important consequence on the detector characteristics.

	r=75 cm	r=85 cm	r=95 cm	r=105 cm	r=115 cm
Charged pions	0.76 ± 0.02	0.54 ± 0.02	0.38 ± 0.02	0.24 ± 0.01	0.152 ± 0.008
Protons	0.146 ± 0.007	0.108 ± 0.007	0.082 ± 0.005	0.057 ± 0.004	0.039 ± 0.003
Charged kaons	0.056 ± 0.006	0.040 ± 0.004	0.033 ± 0.004	0.025 ± 0.005	0.013 ± 0.001
Neutral kaons	0.022 ± 0.002	0.019 ± 0.002	0.014 ± 0.001	0.011 ± 0.001	0.009 ± 0.001
Neutrons (E>100 keV)	1.91 ± 0.05	1.88 ± 0.05	1.86 ± 0.04	1.87 ± 0.06	1.88 ± 0.06
Neutrons (E>20 MeV)	0.41 ± 0.01	0.368 ± 0.009	0.324 ± 0.007	0.307 ± 0.007	0.297 ± 0.06
Neutrons total	9.0 ± 0.2	9.0 ± 0.2	8.9 ± 0.2	8.8 ± 0.2	8.8 ± 0.2
Hadrons ('E>100 keV')	2.90 ± 0.06	2.58 ± 0.05	2.36 ± 0.05	2.20 ± 0.06	2.09 ± 0.06
Hadrons ('E>20 MeV')	1.40 ± 0.03	1.07 ± 0.02	0.83 ± 0.02	0.65 ± 0.01	0.51 ± 0.01
Absorbed dose (kGy)	6.8 ± 0.2	5.0 ± 0.2	3.6 ± 0.1	2.55 ± 0.08	1.85 ± 0.07

Table 21: Longitudinally averaged hadron fluences and absorbed dose in the five layers of the barrel silicon tracker. All values are given as 10^{13} cm^{-2} for an integrated luminosity of 5×10^5 pb^{-1}. The fluence of hadrons 'E>100 keV' is the sum over the first five rows of each column and serves as a good approximation to the 1 MeV neutron equivalent fluence. The indicated errors refer only to the simulation statistics.

	z=117 cm	z=141 cm	z=177 cm	z=210 cm	z=255 cm
Charged pions	0.74 ± 0.06	0.86 ± 0.08	0.78 ± 0.03	0.92 ± 0.07	1.00 ± 0.09
Protons	0.16 ± 0.02	0.25 ± 0.06	0.27 ± 0.04	0.27 ± 0.04	0.27 ± 0.04
Charged kaons	0.06 ± 0.01	0.036 ± 0.009	0.08 ± 0.01	0.06 ± 0.02	0.07 ± 0.01
Neutral kaons	0.034 ± 0.008	0.022 ± 0.006	0.03 ± 0.01	0.021 ± 0.005	0.026 ± 0.006
Neutrons (E>100 keV)	1.9 ± 0.1	2.4 ± 0.2	2.6 ± 0.4	2.6 ± 0.1	3.6 ± 0.2
Neutrons (E>20 MeV)	0.41 ± 0.04	0.49 ± 0.05	0.7 ± 0.2	0.58 ± 0.06	0.74 ± 0.06
Neutrons total	9.9 ± 0.4	10.6 ± 0.4	11.0 ± 0.6	11.9 ± 0.5	13.5 ± 0.4
Hadrons ('E>100 keV')	2.8 ± 0.1	3.6 ± 0.2	3.7 ± 0.4	3.9 ± 0.2	4.9 ± 0.2
Hadrons ('E>20 MeV')	1.41 ± 0.08	1.7 ± 0.1	1.9 ± 0.2	1.9 ± 0.1	2.1 ± 0.1
Absorbed dose (kGy)	6.6 ± 0.6	9 ± 1	8.7 ± 0.6	9.4 ± 0.6	10.3 ± 0.9

Table 22: Hadron fluences at the lowest edges (r=75 cm) of some outer silicon endcap disks. All values are given as 10^{13} cm^{-2} for an integrated luminosity of 5×10^5 pb^{-1}. The fluence of hadrons 'E>100 keV' is the sum over the first five rows of each column and serves as a good approximation to the 1 MeV neutron equivalent fluence. The indicated errors refer only to the simulation statistics.

Fig. 56 shows the expected evolution of the depletion voltage for detectors of various thickness and a resistivity of 3 kΩcm evantually exposed to 7.5×10^{13} hadrons/cm^2, which corresponds to a safety factor of 3 for most regions of the outer tracker. We can notice that, after 10 years of running, even the 500 μ thick sensors will reach low depletion voltages, allowing easily overdepletion. In

addition, the larger part of these detectors will just reach type inversion and will be operated in the second half of the CMS running at depletion voltages below 100 V. This allows us to consider thicker detectors to be used in this part of the tracker.

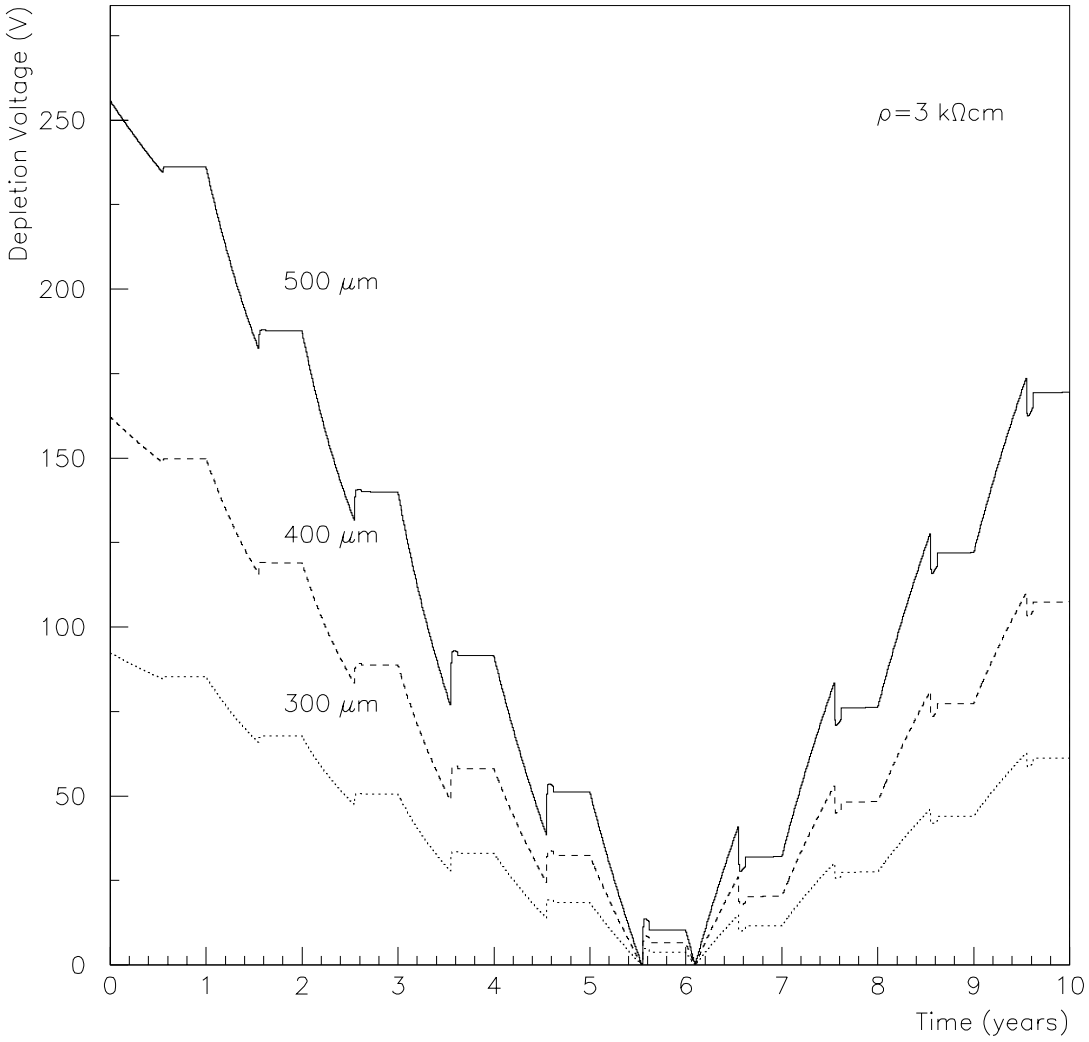

Figure 56: Depletion voltage for silicon detectors of three different thicknesses and a resistivity of 3 k Ωcm as function of LHC years. In these calculations a maintenance scenario with the detector at +10°C during 21 days and at +21°C during 10 days was assumed per year. The final dose of the sensor, after 10 LHC years is 7.5×10^{13} hadrons/cm^2.